

Article

A CFD-Based Surrogate for Pump–Jet AUV Maneuvering

Younhee Kwon ¹, Dong-Hwan Kim ^{1,*}, Jeonghwa Seo ² and Hyun Chung ²

¹ Research Institute of Future Mobility System, Chungnam National University, Daejeon 34134, Republic of Korea; younheekwon@cnu.ac.kr

² Department of Autonomous Vehicle System Engineering, Chungnam National University, Daejeon 34134, Republic of Korea; j.seo@cnu.ac.kr (J.S.); hchung@cnu.ac.kr (H.C.)

* Correspondence: dkbr@cnu.ac.kr

Abstract

Prediction of the maneuvering performance of autonomous underwater vehicles equipped with pump–jet propulsion remains computationally intensive when relying solely on high-fidelity computational fluid dynamics. To overcome this limitation, a surrogate maneuvering model is developed to achieve comparable accuracy with drastically reduced computational cost. The model is constructed from numerical results obtained using unsteady Reynolds-averaged Navier–Stokes equations with the $k-\omega$ shear stress transport turbulence model, and formulated through a Taylor-expansion-based framework. The propulsion and rudder modules are refined to enhance physical representation and efficiency: a conventional open-water-based formulation is adopted to embed the pump–jet propulsive model, incorporating axial flow velocities near the duct inlet for improved thrust prediction; meanwhile, the rudder force model minimizes the number of captive simulations by employing a kinematic approach that compensates for limited datasets. The surrogate model is applied to free-running simulations and validated against high-fidelity computational results. The findings confirm that the proposed framework reproduces the dominant trends of kinematic responses, forces, and moments with high consistency, providing a practical and time-efficient alternative for maneuvering prediction of underwater vehicles equipped with pump–jet propulsion systems.



Academic Editors: Decheng Wan and Simone Mancini

Received: 28 August 2025

Revised: 30 September 2025

Accepted: 18 October 2025

Published: 21 October 2025

Citation: Kwon, Y.; Kim, D.-H.; Seo, J.; Chung, H. A CFD-Based Surrogate for Pump–Jet AUV Maneuvering. *J. Mar. Sci. Eng.* **2025**, *13*, 2014. <https://doi.org/10.3390/jmse13102014>

Copyright: © 2025 by the authors. Licensee MDPI, Basel, Switzerland. This article is an open access article distributed under the terms and conditions of the Creative Commons Attribution (CC BY) license (<https://creativecommons.org/licenses/by/4.0/>).

Keywords: hydrodynamics; computational fluid dynamics; star-ccm; surrogate; autonomous underwater vehicle; pump–jet; propeller open-water test; planar motion mechanism

1. Introduction

Autonomous underwater vehicles (AUVs) have emerged as one of the most actively studied technologies in marine engineering, driven by their versatility across scientific, industrial, and defense applications. Unlike traditional manned or remotely operated systems, AUVs offer persistent and cost-effective operation in hazardous and remote environments, reducing risks to human operators while expanding the scope of underwater exploration. Their capability to operate independently makes them particularly attractive for missions such as seabed mapping, environmental monitoring, infrastructure inspection, and naval reconnaissance [1–3].

Recent years have witnessed rapid advancements in the enabling technologies that underpin AUV design and operation. Improvements in energy storage, including high-density lithium-ion batteries and fuel-cell systems, have significantly extended mission endurance. Progress in propulsion system design, aided by computational fluid dynamics (CFDs) and reduced-order modeling, has enhanced maneuverability and efficiency in

complex hydrodynamic environments. At the same time, miniaturization of high-resolution sensors, such as sonar, optical imaging devices, and chemical probes, has broadened the range of measurable ocean parameters, enabling high-fidelity mapping of physical, chemical, and biological processes [4–6].

A particularly transformative development lies in autonomy and onboard intelligence. Advances in machine learning, adaptive control, and real-time data processing now allow AUVs to make mission-critical decisions under uncertainty, adapt their trajectories to environmental variability, and coordinate as swarms for distributed sensing. These capabilities have expanded the operational horizon of AUVs from coastal monitoring to deep-ocean exploration and under-ice missions, where human access is limited or impossible [7–12].

Beyond technological progress, global challenges have further motivated AUV research. Climate change, biodiversity conservation, and pollution mitigation require sustained, large-scale ocean observation with spatial and temporal resolutions unachievable by conventional ship-based surveys. Similarly, offshore industries and defense operations demand reliable, long-duration platforms for inspection, surveillance, and asset protection. As a result, AUVs are now regarded as indispensable tools for addressing both fundamental scientific questions and pressing societal needs [13,14].

In this context, the development of robust motion prediction models and surrogate frameworks is critical for ensuring the safe, efficient, and autonomous operation of AUVs. High-fidelity CFD simulations, serving as a complementary counterpart to costly experiments, provide detailed insights into the complex flow physics of propulsion and maneuvering while requiring only the physical geometry at the early design stage. However, their computational expense limits applicability to long-duration trajectory prediction and to identifying appropriate control parameters, for which no effective solution has yet been established. For example, even tuning PID gains for a course-keeping simulation requires a large number of runs. Reduced-order models, surrogate approaches, and hybrid strategies have therefore become central research directions, bridging the gap between accuracy and computational efficiency by leveraging high-fidelity solutions.

The present study contributes to this ongoing effort by developing and validating a surrogate motion prediction model for a pump-jet-propelled AUV, with a focus on balancing fidelity and practicality for free-running simulations [15–17]. While most reduced-order modeling studies on AUVs focus on validating maneuvering coefficients within a whole-ship framework [18–21], this study advances by coupling the surrogate with kinematic relations and a limited set of empirical values that capture the essential physics. This approach reduces preparation effort, enhances physical interpretability, and enables the identification of factors that yield predictive accuracy comparable to free-running results from high-fidelity simulations, owing to its transparent and traceable structure. Another key contribution of this work is the surrogate modeling of the pump-jet propulsion module. The AUV considered employs a ducted propeller that enhances propulsive efficiency and suppresses cavitation, making it well-suited for low-speed, high-thrust operations. The duct also mitigates propeller damage from debris during full-scale deployment. There are only a few recent studies that have attempted a similar approach. A body-force module for a ducted ship propeller is modeled, matching thrust coefficients between POW tests conducted with and without the duct [22]. Also, a modified body-force approach for CFD simulation of a pump-jet-propelled AUV is proposed, where an empirical factor was obtained from steady-state simulations with a discretized propeller to adjust the advance coefficient [23]. Because the empirical factor was derived from the hull-propeller system, it implicitly incorporated both the duct-accelerated flow and the wake fraction. In the present study, by contrast, the framework is based directly on POW results and does not rely on a non-ducted propeller reference. In addition, the empirical factor here is extracted

directly from the POW test and modularized for use in the surrogate model. Beyond the surrogate, the same abstraction enables a computationally efficient CFD setup using a body-force representation, offering practical computation times while preserving essential propulsive characteristics.

The following chapters present the following: Principal particulars of AUV are presented in Section 2. The CFD framework, including the computational setup, test matrix, and governing equations, is described in Section 3. Section 4 presents the methodology for constructing the surrogate model. The construction of a surrogate model based on CFD simulations is described in Section 5, while Section 6 discusses the free-running capability of the surrogate model. Finally, conclusions are summarized in Section 7.

2. Target AUV Model

2.1. Main Particulars

As shown in Figure 1, the 2 m class AUV used in this study, built by the LIG Nex1 corporation, is a recently constructed vehicle designed with diverse free-running missions in mind. Table 1 presents the principal specifications of the AUV.



Figure 1. Actual 2 m class AUV model used in the present study.

Table 1. Main principals (fully attached AUV).

Description	Symbol	Factor ¹	Value ²
Breadth	B	L	0.074
Mass	m	ρL^3	3.830×10^{-3}
Center of gravity ³ (x-dir., from nose)	x_G	L	0.463
Radius of gyration (z-dir., from COG)	k_z	L	0.166
Moment of inertia (z-dir., from COG)	I_z	ρL^5	1.059×10^{-4}
Location of rudder axis ³ (x-dir., from nose)	x_R	L	0.904
Location of propeller center ³ (x-dir., from nose)	x_P	L	0.982
Propeller diameter	D_P	L	0.063

¹ Factor for non-dimensionalization. $\rho = 998 \text{ [kg/m}^3\text{]}$ is used; ² dimensionless value; ³ distance from the nose of AUV.

The mass and center of gravity (COG) of the AUV are obtained from CFD hydrostatic simulations without the use of design variables. The COG is defined as the distance measured from the foremost point of the AUV. The radii of gyration and moments of inertia (MOI) are estimated based on design variables, with the COG as the reference point. The overall configuration of the AUV used for the computation is shown in Figure 2a. The holes distributed along the hull, as shown in Figure 2a, are designed as mounting slots for vertical and horizontal thrusters. In this study, however, the thrusters themselves are not modeled in either the CFD simulations or the surrogate model, and only the holes remain in the geometry.

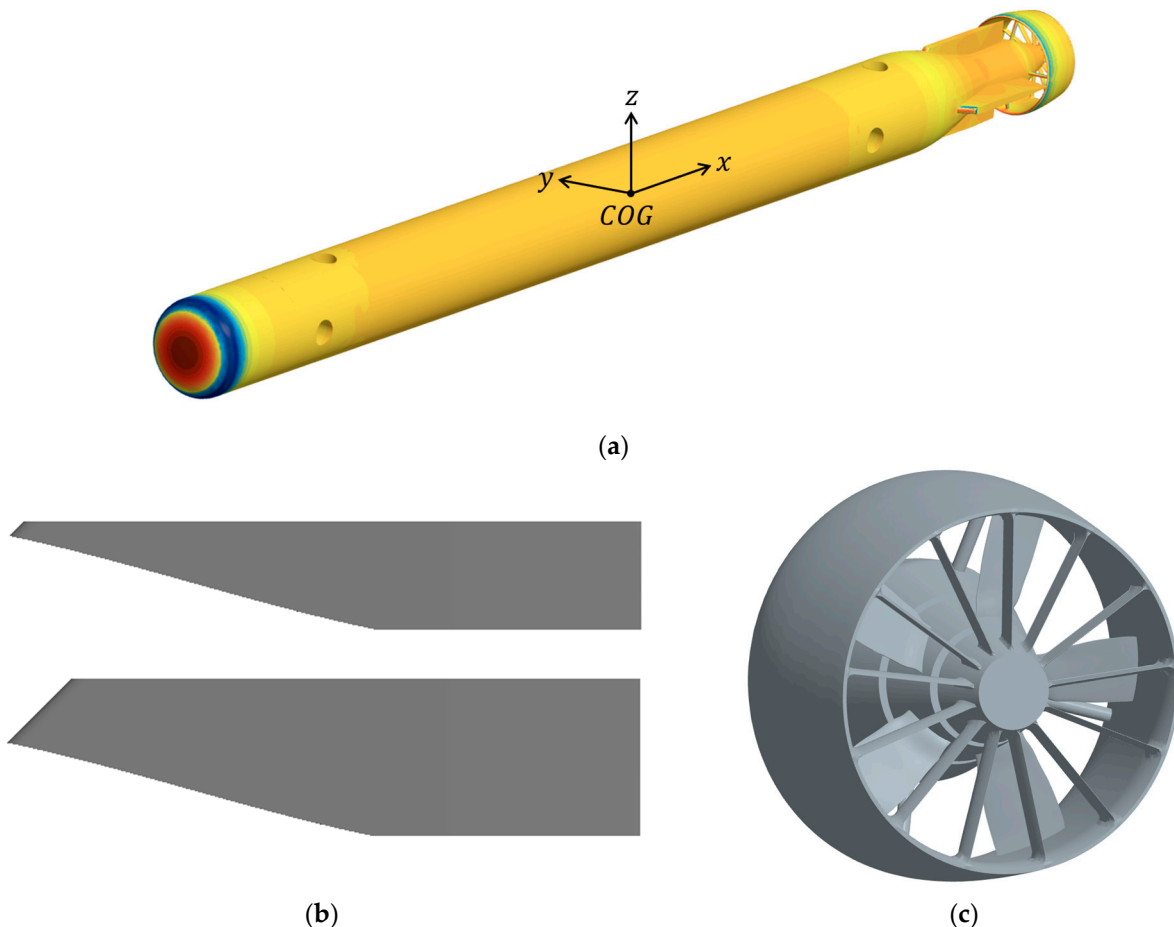


Figure 2. Target AUV model geometry for the computation: (a) fully appended AUV; (b) vertical (up) and horizontal (down) rudders; (c) propulsion region showing both duct and propeller blades. The clearance between the propeller rotor and AUV hull's tail part is intentionally imposed to facilitate CFD computation.

The rudders are designed such that the spans of the port and starboard rudders are larger than those of the vertical rudders in order to enhance controllability in the horizontal plane (Figure 2b). Since this study focuses on horizontal-plane maneuvering, only the vertical rudder span is listed in the table. It is also noted that the rudders have relatively small spans compared to the AUV's length due to its capability to be launched from a tube. The propeller duct is supported by four upstream and thirteen downstream struts, arranged in an axisymmetric manner (Figure 2c). The propeller consists of five axisymmetric blades.

2.2. Coordinate System

This study employs two coordinate systems with parallel axes but different origins in both the CFD and surrogate formulations: the earth-fixed frame and the body-fixed frame. The origin of the earth-fixed frame is located at the geometric center of the AUV's nose, while the origin of the body-fixed frame coincides with the center of gravity. Since the present study focuses on 3 degrees of freedom (DOF) motion, the earth-fixed frame is used to compute translational displacements in the body-fixed frame, namely, surge (x), sway (y), and yaw (ψ), and to measure the longitudinal offset of the COG from the AUV's nose. The axes are defined such that the +x axis points toward the tail, the +y axis points to starboard, and the +z axis points upward.

3. CFD

3.1. URANS

In this study, the incompressible URANS equations are numerically solved using an unstructured grid-based finite volume method (FVM). The commercial CFD solver STAR-CCM+ V2302 (Siemens Digital Industries Software, Plano, TX, USA) is employed. Equation (1) presents the governing equations of incompressible URANS:

$$\frac{\partial \bar{v}}{\partial t} + \nabla \cdot [(\bar{v} - v_g) \otimes \bar{v}] = -\nabla \bar{p}/\rho + (\nu + \nu_t) \nabla^2 \bar{v} \quad (1)$$

where v , p , ν , and ν_t denote the flow velocity, piezometric pressure, kinematic viscosity, and eddy viscosity, respectively, and upper bar indicates Reynolds-averaged quantities. When the grid at certain coordinate system moves with both translational and rotational speed, with respect to other coordinate system, the grid velocity (v_g) is defined as Equation (2):

$$v_g = v_{g,t} + \omega_g \times r \quad (2)$$

where $v_{g,t}$ is the translational velocity vector of the grid, ω_g is the rotational velocity vector of the grid, and r is the position vector of a mesh vertex.

3.2. Turbulence Model

The current simulations employ Menter's SST $k - \omega$ SST model [24], an anisotropic two-equation turbulence model based on the eddy-viscosity formulation, for turbulence closure.

In ship applications, the $k - \omega$ SST model is predominantly used, whereas in AUV numerical simulations, the two major candidates, $k - \varepsilon$ and $k - \omega$ SST, were both employed, and transition modeling is also of concern. Transition effects are particularly crucial for AUVs compared to ships, since the resultant hydrodynamic forces have a proportionally greater influence on the vehicle's motion, especially near the free surface [25,26] and on propulsor performance [27]. This is attributed to the fact that AUVs are generally smaller than model-scale ships and possess significantly lower pitch and yaw moments of inertia than ships.

Since the transition model is not included in the present study, the $k - \omega$ SST model is employed to provide more accurate predictions of flows with adverse pressure gradients than the $k - \varepsilon$ model. It should be noted, however, that the influence of transition modeling on AUV hydrodynamics remains a crucial issue, as the vehicle's motion is highly sensitive to laminar-turbulent transition effects.

3.3. Numerical Schemes

For temporal discretization, the second-order implicit backward differentiation that incorporates five time levels is used. Convective fluxes of momentum equations and transport equations for turbulence variables are computed with the second-order upwind scheme. Diffusive fluxes are dealt with the central differencing scheme formulated with non-orthogonality adjustment terms, namely, the cross-diffusion terms. Gradients are computed with the Gauss linear method with Venkatakrishnan limiter. For pressure-velocity coupling, a semi-implicit method for pressure-linked equations (SIMPLE) algorithm is used. The implemented blended wall-functions are used as near-wall treatments for velocities, k , and ω_t .

3.4. Equations of Motion

In predicting the motion of a moving body, the key quantities obtained from the fluid field are the forces and moments acting on the body. The shear stresses and pressure forces

derived from the discretization of Equation (1) are ultimately computed in the earth-fixed coordinate system. On the other hand, when the body accelerates in a non-inertial frame, the governing equations of motion can be formulated based on Newton's second law with respect to the body-fixed coordinate system, as shown in Equation (3) [28,29]:

$$m[\dot{u} - vr + wq - x_{rg}(q^2 + r^2) + y_{rg}(pq - \dot{r}) + z_{rg}(pr + \dot{q})] = X \quad (3a)$$

$$m[\dot{v} - wp + ur - y_{rg}(r^2 + p^2) + z_{rg}(qr - \dot{p}) + x_{rg}(qp + \dot{r})] = Y \quad (3b)$$

$$m[\dot{w} - uq + vp - z_{rg}(p^2 + q^2) + x_{rg}(rp - \dot{q}) + y_{rg}(rq + \dot{p})] = Z \quad (3c)$$

$$I_x \dot{p} + (I_z - I_y)qr + m[y_{rg}(\dot{w} - uq + vp) - z_{rg}(\dot{v} - wp + ur)] = K \quad (3d)$$

$$I_y \dot{q} + (I_x - I_z)rp + m[z_{rg}(\dot{u} - vr + wq) - x_{rg}(\dot{w} - uq + vp)] = M \quad (3e)$$

$$I_z \dot{r} + (I_y - I_x)pq + m[x_{rg}(\dot{v} - wp + ur) - y_{rg}(\dot{u} - vr + wq)] = N \quad (3f)$$

where u, v, w, p, q, r and $\dot{u}, \dot{v}, \dot{w}, \dot{p}, \dot{q}, \dot{r}$ are 6DOF velocity and acceleration components; X, Y, Z, K, M, N are 6DOF force and moment components; and I_x, I_y, I_z are principal components of moment of inertia tensor of a moving body defined in the body-fixed coordinate. The reference point of moments of inertia is the center of rotation, which is assumed the same as center of gravity in this study. x_{rg}, y_{rg}, z_{rg} are the components of distance vector pointing center of gravity from center of rotation; thus, they are all zero values in the current study. Due to the relative reference between the inertial and non-inertial frames, apparent inertial effects such as the Coriolis forces ($m(p, q, r) \times (u, v, w)$) arise in the non-inertial coordinate system. For the 3DOF computation, corresponding to the final free-running condition, Equation (3) can be simplified to Equation (4).

$$m(\dot{u} - vr) = X \quad (4a)$$

$$m(\dot{v} + ur) = Y \quad (4b)$$

$$I_z \dot{r} = N \quad (4c)$$

Through Euler angles, kinematic variables obtained in each coordinate system can be transformed between the inertial and non-inertial frames. However, since the moments of inertia remain constant in the body-fixed frame, and in the surrogate model all quantities, except for trajectory prediction, are considered in the body-fixed frame, the formulation of the equations of motion in the body-fixed coordinate system is more straightforward in both conceptual and computational aspects.

3.5. Grid-Dependency Test

This study verifies grid resolution for both propeller characteristics and hull resistance. Instead of evaluating uncertainties through Richardson extrapolation, a more practical approach is adopted by constructing three grid systems with different resolutions and examining the relative differences in the solutions with respect to grid convergence. Richardson extrapolation often exhibits oscillatory convergence behavior. Such oscillations are considered not to originate from the overset methodology itself, but rather from the fact that the employed grid sizes are already close to the asymptotic solution.

3.6. Grid System

Since the present study focuses exclusively on the AUV in a fully submerged condition without free-surface effects, the background grid is configured to move together with the body. Local mesh refinement is applied in regions where strong pressure gradients

are expected, such as the nose and stern with rudders, where the cell size is reduced to one-half or one-quarter of the cell size located at mid-body. Around the propeller, an even finer refinement of up to one-eighth of the mid-body size is employed (Figure 3). In the mid-body region, the longitudinal grid size is approximately 0.0141 m in the G2 mesh system. The background grid is designed to gradually expand away from the mid-body, reaching up to eight times the mid-body cell size. For the boundary layer, a near-wall spacing of approximately 6.0×10^{-4} m is applied around the hull, including appendages.

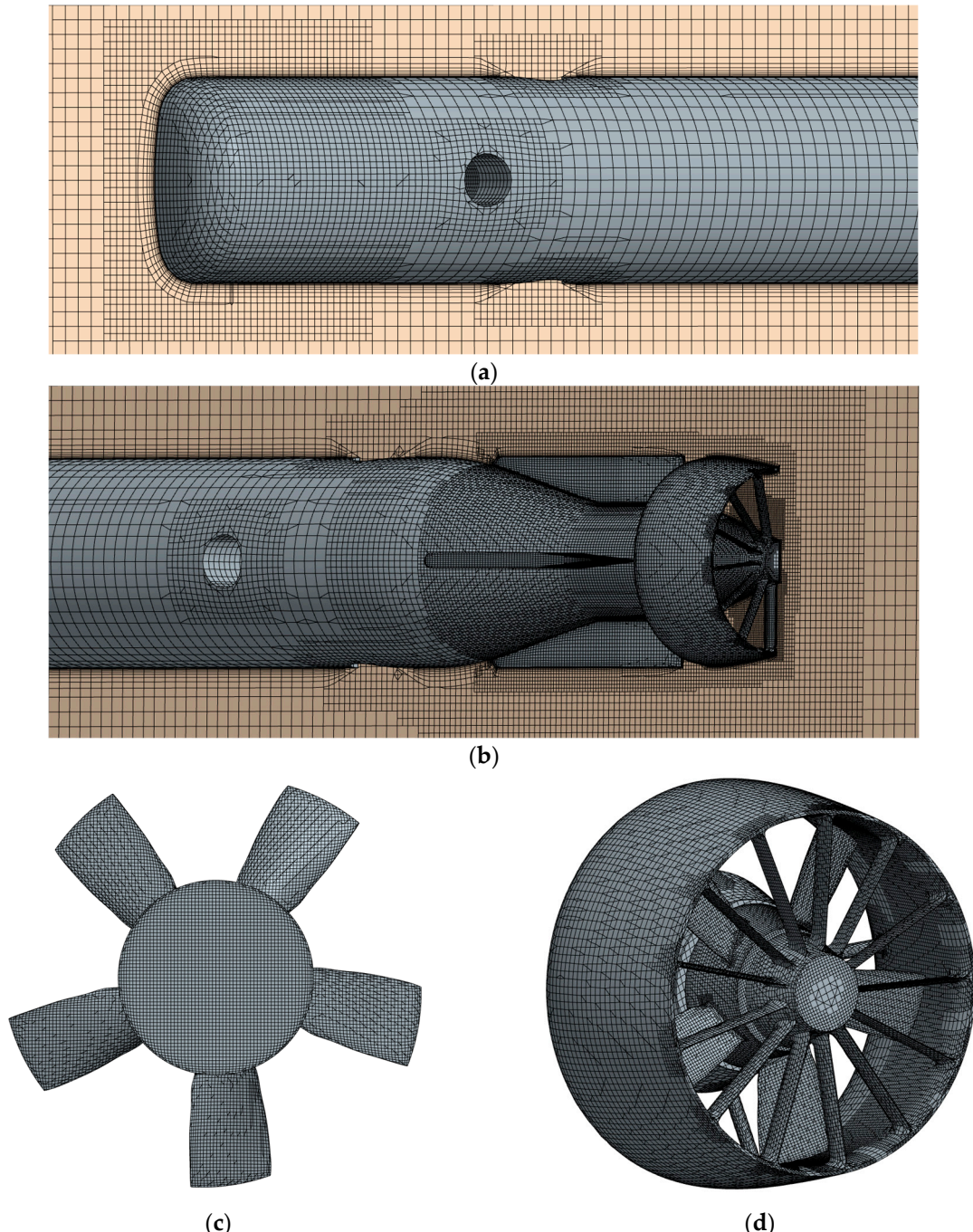


Figure 3. Surface grids on AUV and $y = 0$ plane: (a) near AUV nose; (b) near stern; (c) propeller blades; (d) propulsion system including a duct and struts.

The four rudders, each moving with 1DOF, and the propeller are allowed to move relative to the hull. To achieve this, grid separation between the hull and appendage

meshes is required. An overset grid approach is used such that the rudders and propeller are embedded within the hull and duct grid systems, while the duct is unified with the hull via struts. Boundary values between overset regions are interpolated linearly (Figure 4). Overset interfaces are also applied between rudder regions due to their mutual interference.

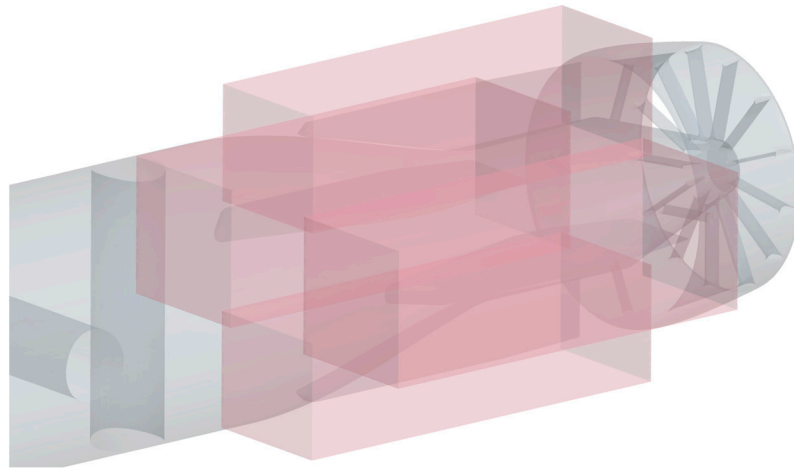


Figure 4. Overset configuration demonstration: overset regions for 4 rudders (shaded in red) are shown.

As aforementioned, the entire grid system is prepared at three different resolutions. Starting from the baseline G1 mesh, coarser meshes G2 and G3 are generated by increasing the characteristic grid size by a factor of $\sqrt{2}$ successively. Two grid triplet sets are constructed: one for the propeller open-water (POW) test and another for the remaining simulations, including hull and rudders. The corresponding numbers of grid points are listed in Tables 2 and 3, respectively.

Table 2. Number of grid points of grid triplet for POW simulation.

Region	# of Cells [M]		
	G1	G2	G3
Blade	0.79	0.41	0.24
Duct	1.67	0.83	0.46
Background	0.07	0.04	0.03
Total	2.53	1.28	0.73

Table 3. Number of grid points of grid triplet for simulations, including hull and rudders.

Region	# of Cells [M]		
	G1	G2	G3
Hull *	3.02	1.47	0.78
Rudders	0.86	0.35	0.14
Background	0.17	0.07	0.03
Total	4.05	1.89	0.95

* includes duct.

3.7. Domain, Boundary Conditions, and Initial Conditions

Figure 5 shows the computational domain, and Table 4 summarizes the boundary conditions. For the POW test, only the duct and propeller are included, as illustrated in Figure 3d, and the domain size is scaled by $L/(10D_P)$. In general, background grid boundaries impose streamwise (U) and transverse (V) velocities, and the flow field inside the domain is initialized with the same velocities. In simulations where the body undergoes

prescribed displacements, namely, forced oscillation, pure sway, pure yaw, and zigzag tests, zero inflow conditions ($U = V = 0$) are applied at the boundaries, and the initial conditions are all set to zero. In these cases, the forces acting on the hull are computed in terms of the relative velocity obtained from the equations of motion.

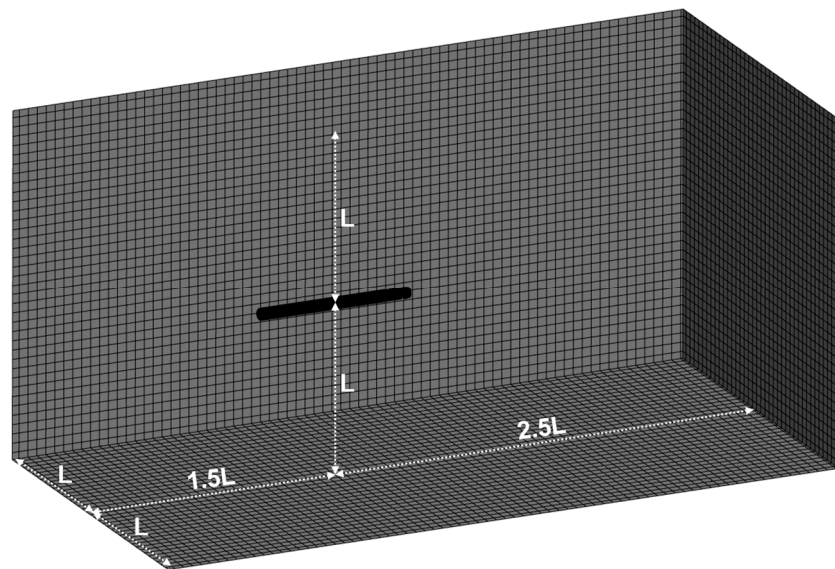


Figure 5. Computation domain size.

Table 4. Boundary conditions.

BC	$\bar{u}, \bar{v}, \bar{w}$	p	k^*	ω
Inlet	$(U, V, 0)$	Extrapolated	$\frac{3}{2}(0.01U_I)^2$	$\frac{\rho k}{10}$
Exit	Extrapolated	Extrapolated	Zero-gradient	Zero-gradient
Wall	Grid velocity	Zero-gradient	Zero-gradient	Zero-gradient

$$* U_I = \sqrt{U^2 + V^2}.$$

3.8. Body-Force Propulsion

In this study, the POW simulations are first conducted using a discretized propeller (DP), and the obtained POW characteristics, i.e., thrust coefficient $K_T (= X / (\rho n^2 D_P^4))$ and torque coefficient $K_Q (= K / (\rho n^2 D_P^5))$, are subsequently employed to establish a body-force (BF) propulsion model for the free-running simulations. The distribution of the body-force components are set to follow Goldstein's optimum distribution. Since the propeller located inside the duct induces a local acceleration of the flow near the duct inlet, the averaged axial propeller inflow speeds at the duct inlet (u_A) are measured at a cross-section (Figure 6) in the discretized propeller simulations and utilized to formulate the advance coefficient at the duct inlet ($J_A = u_A / (nd)$) rather than utilizing the advance coefficient based on ship speed ($J = u / (nd)$). Based on these measurements, an additional correlation (Equation (5)) between J and J_A is derived, ensuring that the thrust and torque coefficients could be properly adjusted to act with respect to the hull-relative velocity. While the present study employs a second-order polynomial for regression of the propeller's hydrodynamic performance, the use of higher-order polynomials may also be recommended when improved accuracy is required.

$$J_A = J_1 J + J_0 \quad (5a)$$

$$K_T = K_{T0} + K_{T1} J_A + K_{T2} J_A^2 \quad (5b)$$

$$K_Q = K_{Q0} + K_{Q1} J_A + K_{Q2} J_A^2 \quad (5c)$$

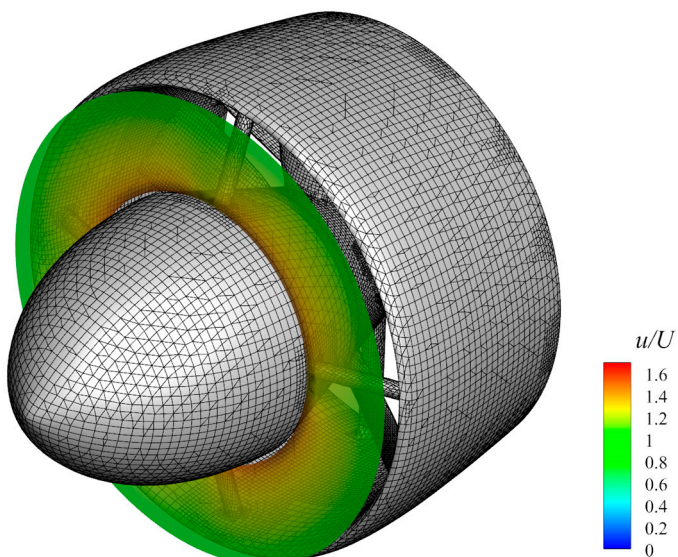


Figure 6. Sectional area for obtaining average axial speed at the duct inlet.

3.9. Controller

In the free-running simulations, a controller is required to compute and adjust the vertical rudder angle (δ) at each time step based on the yaw motion (ψ) of the AUV. In this study, the yaw angle reported at every time step is linked to a JavaScript-based macro, which calculates the corresponding rudder angle. The computed rudder angle is then fed back into STAR-CCM+ through a field function to rotate the rudder mesh accordingly.

4. Surrogate

The main purpose of the surrogate model is to retain the accuracy of CFD while significantly reducing the computational cost. To achieve this, it is advantageous for the surrogate to adopt modules as similar as possible to those used in CFD, enabling transparent error tracking. The surrogate is therefore designed to employ the same coordinate system and input variables, as well as the same equation of motion and rudder controller. The only distinction lies in the estimation of forces and moments.

While the CFD solver requires only the inputs listed in Table 1 and the discretized geometry for meshing, the surrogate further modularizes the force and moment estimation. Accordingly, in addition to the values in Table 1, additional inputs specific to force and moment estimation are required. These inputs are detailed in the following section, where the governing expressions for forces and moments are presented.

4.1. Algorithm

Figure 7 presents the algorithmic flowchart of the surrogate model used in this study. The surrogate performs calculations at a certain time step using the AUV velocity variables updated from the accelerations of the previous time step; at the first time step, the initialized velocity values are used. At the beginning of each timestep, the calculation starts with determining the effective inflow speed and drift angle of the hull. Using these values, forces and moments are obtained from a pre-regressed Taylor expansion expression. The estimated forces and moments are then substituted into the equation of motion, from which new accelerations and velocities are computed.

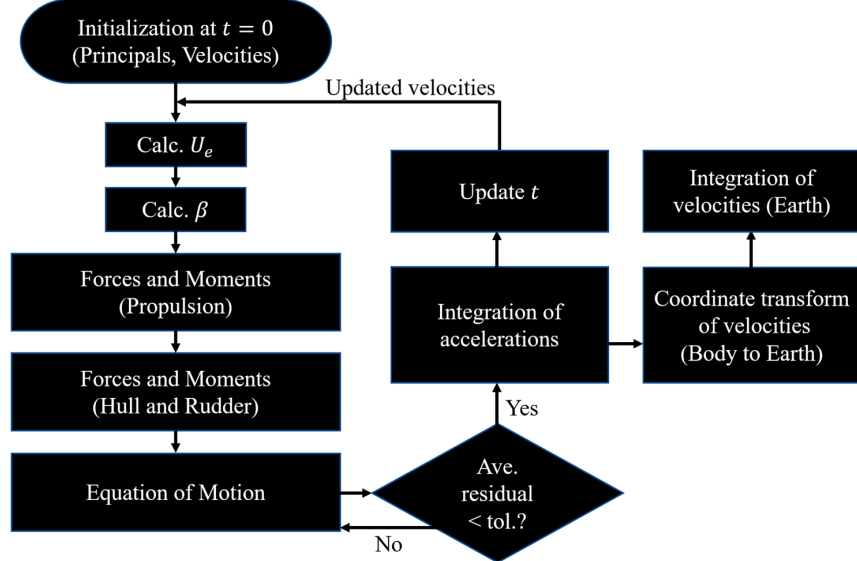


Figure 7. Surrogate algorithm flowchart.

Separately from the force and moment evaluation, the trajectory is determined. As in CFD, the velocities computed from the equation of motion defined in the non-inertial coordinate system are transformed into the inertial coordinate system and integrated to obtain the trajectory. In the force and moment calculation, the propeller loads are computed prior to those of the hull and rudders, since a portion of the propeller thrust contributes to the hull through the thrust-deduction effect.

Although the general form of the equations of motion is identical to that in CFD, the present surrogate employs a nonlinear iterative scheme. The following subsections present the detailed formulations involved in each module.

4.2. Effective Flow Speed

The effective flow speed for scaling maneuver coefficients and kinematic properties is defined as follows:

$$U_e = \sqrt{u^2 + v^2} \quad (6)$$

4.3. Hull Drift Angle

The drift angle of the hull for estimating the incident angle of the rudder and propeller is defined as follows:

$$\beta = \tan^{-1}(-v/u) \quad (7)$$

4.4. Forces and Moments—Propulsion

A propulsion model based on the POW curves is established by adopting the propeller force and moment module from the standard MMG formulation [30]. In addition, the correlation between the AUV-relative velocity and the duct inflow velocity obtained from the CFD body-force propulsion approach (Equation (5)) is incorporated once the advance coefficient is obtained via Equation (8c).

$$\beta_P = \beta + (x_P/L)(\psi L/U_e) \quad (8a)$$

$$\omega_P = \omega_0 - \exp(-25\beta_P^2) \quad (8b)$$

$$J = u(1 - \omega_P)/(nD_P) \quad (8c)$$

where β_P , ω_P , ω_0 , and n are incident angle toward the propeller, wake fraction of the propeller inflow in the oblique flow, wake fraction of the propeller inflow in the straight flow, and propeller rotational speed, respectively. The thrust coefficient obtained by Equation (5) with Equation (8c) is used to estimate the dimensional thrust of the propeller as follows:

$$X_P = \rho n^2 D_P^4 K_T \quad (9)$$

4.5. Forces and Moments—Hull and Rudder

The hull and rudder force/moment module employs a whole-ship approach [31] and applies the angle of attack of the rudder (α) formulation for oblique flow (Equation (10b)), which is aimed at reducing the number of simulations needed to obtain forces and moments when drift angle and rudder deflection occur simultaneously.

$$\beta_R = \beta + (x_R/L)(\psi L/U_e) \quad (10a)$$

$$\alpha = \delta - \tan(\beta_R) \quad (10b)$$

The resistance is formulated to be the function of surge speed as follows:

$$R = R_0 + R_1 u + R_2 u^2 \quad (11)$$

The final form of forces and moment of hull and rudder comprises the effect of sway velocity (v), sway acceleration (\dot{v}), yaw rate (r), yaw acceleration (\dot{r}), and δ in a Taylor-expansion form [28].

$$X_H = F \left(-R + X_{vv} v'^2 + X_{vvvv} v'^4 + X_{vvvvvv} v'^6 + X_\delta |\alpha| + X_{\delta\delta} \alpha^2 \right) + t_p X_P \quad (12a)$$

$$Y_H = F \left(Y_v v' + Y_{v|v|} v' |v'| + Y_{vvv} v'^3 + Y_\delta \alpha + Y_{\delta|\delta|} \alpha |\alpha| + Y_{\delta\delta\delta} \alpha^3 + Y_{\dot{v}} \dot{v}' + Y_r r' + Y_{r|r|} r' |r'| + Y_{\dot{r}} \dot{r}' \right) \quad (12b)$$

$$N_H = FL \left(N_v v' + N_{v|v|} v' |v'| + N_{vvv} v'^3 + N_\delta \alpha + N_{\delta|\delta|} \alpha |\alpha| + N_{\delta\delta\delta} \alpha^3 + N_{\dot{v}} \dot{v}' + N_r r' + N_{r|r|} r' |r'| + N_{\dot{r}} \dot{r}' \right) \quad (12c)$$

where the kinematic variables are expressed in non-dimensional form ($v' = v/U_e$, $r' = rL/U_e$, $\dot{v}' = \dot{v}L/U_e^2$, $\dot{r}' = \dot{r}L^2/U_e^2$) with the non-dimensional representation of forces and moments, which are scaled by $F = (0.5)\rho L T U_e^2$ and FL , respectively. t_p denotes the thrust deduction factor. As with the nature of a Taylor-series expansion, each term multiplied by a maneuvering coefficient represents the contribution in the direction of its corresponding variable at a point in the multivariate space. When extracting coefficients from CFD, we assume conditions in which the influences of other terms are absent. Accordingly, the terms in v and its higher-order powers are obtained from static drift simulations where only v is applied; the terms in δ and its higher-order powers from control-fin simulations where only δ acts; the terms in \dot{v} from pure sway simulations; and the terms in r and its higher-order powers, as well as \dot{r} , from pure yaw simulations. The basis for the regression is chosen heuristically, following common practice whereby the surge force is represented as an even function of sway velocity, while the sway force and yaw moment are represented as odd functions of sway velocity and yaw rate, leading to up to third-order fitting of sway force and yaw moment with respect to sway velocity. In contrast, the surge force is fitted up to sixth order, presumably due to the geometric complexity introduced by the duct. The yaw-rate effect appears to be sufficiently captured by terms up to $r' |r'|$, while the contributions of sway acceleration and yaw acceleration are adequately represented by

linear functions. The thrust deduction factor is evaluated from self-propulsion simulations, since it can only be identified in self-propulsion.

4.6. Equations of Motion

3DOF equations of motion consistent with the CFD framework are employed. Since the forces and moment modeled in the surrogate framework consider quasi-static values, the equations of motion, which artificially include the effect of added masses (m_x, m_y) and the added moment of inertia (J_z), as presented in Equation (13), are used [28]. Once the external forces and moment are obtained with the updated kinematic variables from the previous time step using Equations (9) and (12), the kinematic variables for the current time step are sequentially updated through nonlinear iteration, in which the surge, sway, and yaw motions are converged sequentially, until convergence is achieved, yielding the final accelerations. The convergence tolerance is defined such that the average residual falls below 10^{-10} . The accelerations are then integrated with first Euler method to derive the velocities.

$$(m + m_x)\dot{u} - (m + m_y)vr = X_H + X_P \quad (13a)$$

$$(m + m_y)\dot{v} + (m + m_x)ur = Y_H \quad (13b)$$

$$(I_z + J_z)\dot{r} = N_H \quad (13c)$$

5. Construction of Surrogate Based on CFD Results

Table 5 summarizes the types of CFD simulations conducted to construct the surrogate model and includes the final zigzag simulation for validation after surrogate construction. In this study, the autonomous underwater vehicle is assumed to operate under deep-sea conditions in all cases. To evaluate the accuracy of hull and propeller force and moment simulations, the grid triplet is employed, while the medium grid is used for other simulations. In the POW test with the discretized propeller, a time step of 2.5×10^{-4} s, equivalent to 1.3 degrees per time step, is applied, whereas all other simulations, including those with the surrogate model, use a time step of 0.01 s, which is considered sufficiently small to resolve the time scale of the 2 m class vehicle. The basic composition of the test matrix follows the procedure described in [32].

Table 5. Simulation test matrix.

Simulation	Condition	Grid System
Hydrostatic	Static	G2
POW (discretized)	$J = 0.1\text{--}1.0$	G1, G2, G3
POW (body-force)	$J = 0.1\text{--}1.0$	G2
Resistance	$Fn = 0.097, 0.19, 0.29, 0.39, 0.48$	G1, G2, G3
Self-propulsion ¹	$Fn = 0.39$	G2
Static drift	$\beta = 2, 5, 10, 15, 20, 25$ [deg]	G2
Control-fin	$\delta = 2, 5, 10, 15, 20, 25$ [deg]	G2
Pure sway	$y = (0.1) \sin(0.5\pi t)$, $Fn = 0.39$	G2
Pure yaw ²	$\psi = (0.1/x_g) \cos(0.5\pi t)$	G2
Forced oscillation	$y = (0.1) \sin(\pi t)$, $Fn = 0$	G2
Zigzag ¹	$\delta = +20/20$	G2

¹ Simulation performed with propulsion; ² conditions for y and Fn are identical to those of pure sway.

5.1. Hydrostatic

A hydrostatic simulation was carried out with the AUV fixed and the relative inflow velocity set to zero in order to determine the mass of the fully attached AUV and the longitudinal center of gravity (x_G). Although mass and x_G are often provided from experiments, in this study, they are derived directly from the simulated geometry to ensure

an internal balance between buoyancy and weight, as well as a zero trim moment. Since most simulations are performed under captive conditions and the free-running cases are limited to 3DOF motion, x_G does not affect the vehicle's attitude. However, as it serves as the effective center of rotation and the reference for moments, the x_G obtained from the hydrostatic analysis is consistently employed in the subsequent simulations to improve the prediction of yaw moments. x_G is determined iteratively within the hydrostatic simulation by adjusting its position until the trim moment converges to zero. The final values of mass and x_G are presented in Table 1.

5.2. Propeller Open-Water Test

In the POW test, the hydrodynamic characteristics are obtained from simulations with a discretized propeller under straight-ahead conditions (Figure 8) and subsequently adapted for both the body-force representation in CFD and the surrogate propulsion module. Figure 9 and Tables 6–8 present the thrust coefficient, torque coefficient, and propeller open-water efficiency $\eta_0 (= JK_T / (2\pi K_Q))$ computed from the grid triplet. The results show that the solutions converge toward nearly asymptotic values as the grid resolution increases. The propeller open-water efficiency, a secondary variable derived from the combination of thrust and torque coefficients, exhibited larger discrepancies as it accumulates the errors of both variables. The G3 result for duct resistance indicates a strong sensitivity to grid resolution (Figure 9d). It remains to be investigated whether this error originates from the resolution of the duct surface itself or from the internal flow within the duct, where the pressure drop is induced by the propeller blades. Among the three grids, the G2 case, which provides a median value for computational cost and accuracy, is considered suitable for subsequent body-force modeling.

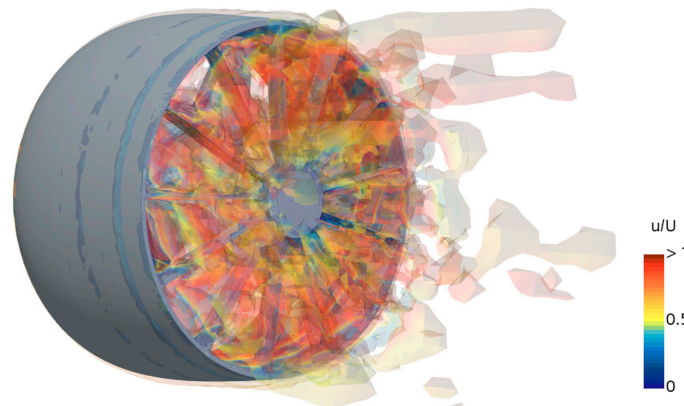


Figure 8. Propeller wake in POW simulation with a discretized propeller model ($Q = 10$).

Table 6. K_T results from POW simulations using grid triplets with the DP model.

J	s_1	s_2	s_3	$\varepsilon_{21} [\%s_1]$	$\varepsilon_{32} [\%s_1]$	R
0.1	0.346	0.342	0.348	-1.1	1.6	-0.72
0.2	0.315	0.313	0.324	-0.7	3.5	-0.2
0.3	0.29	0.288	0.292	-0.8	1.5	-0.51
0.4	0.266	0.257	0.259	-3.3	0.6	-5.04
0.5	0.241	0.231	0.233	-3.8	0.5	-7.11
0.6	0.213	0.207	0.208	-2.8	0.4	-7.91
0.7	0.184	0.179	0.177	-2.7	-1.2	2.25
0.8	0.15	0.144	0.141	-4.3	-1.9	2.24
0.9	0.11	0.104	0.1	-5.8	-3.2	1.82
1	0.065	0.06	0.057	-8.3	-4.8	1.73
Ave. *				3.4	1.9	

* absolute average.

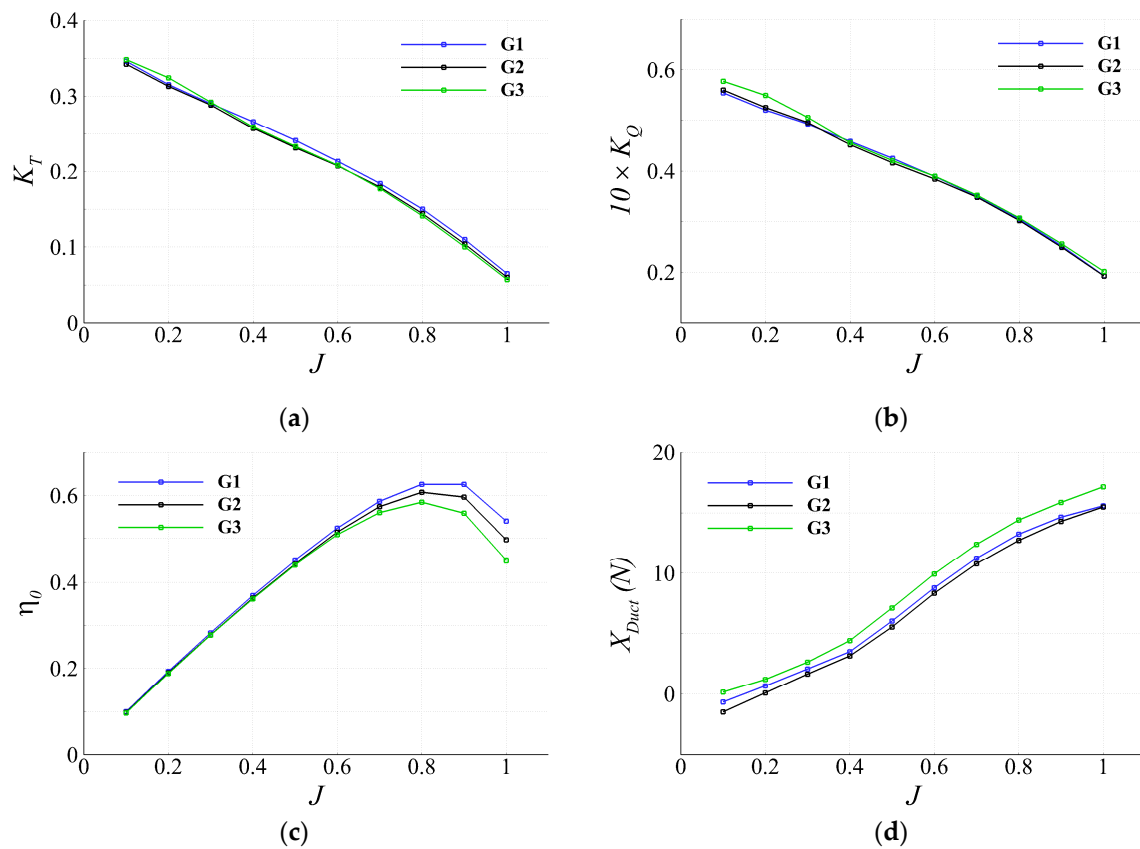


Figure 9. POW characteristic curves obtained via grid triplets of discretized propeller model: (a) thrust coefficient; (b) torque coefficient; (c) propeller open-water efficiency; (d) duct resistance.

Table 7. K_Q results from POW simulations using grid triplets with the DP model.

J	s_1	s_2	s_3	$\varepsilon_{21} [\%s_1]$	$\varepsilon_{32} [\%s_1]$	R
0.1	0.0554	0.056	0.0577	1	3.1	0.33
0.2	0.052	0.0525	0.0549	1	4.6	0.22
0.3	0.0492	0.0495	0.0505	0.6	2.1	0.29
0.4	0.0459	0.0452	0.0456	-1.6	1	-1.63
0.5	0.0425	0.0416	0.0421	-2.1	1.1	-1.81
0.6	0.0389	0.0384	0.039	-1.2	1.5	-0.79
0.7	0.035	0.0348	0.0352	-0.8	1.2	-0.65
0.8	0.0305	0.0302	0.0307	-1.2	1.8	-0.66
0.9	0.0252	0.0249	0.0256	-1	2.9	-0.35
1	0.0193	0.0192	0.0201	-0.5	4.7	-0.1
Ave.				1.1	2.4	

Table 8. η_0 results from POW simulations using grid triplets with the DP model.

J	s_1	s_2	s_3	$\varepsilon_{21} [\%s_1]$	$\varepsilon_{32} [\%s_1]$	R
0.1	0.099	0.097	0.096	-2.1	-1.4	1.54
0.2	0.193	0.19	0.188	-1.7	-1	1.77
0.3	0.282	0.278	0.277	-1.4	-0.5	2.95
0.4	0.369	0.363	0.361	-1.7	-0.3	5.1
0.5	0.45	0.442	0.44	-1.8	-0.6	3.03
0.6	0.524	0.515	0.509	-1.6	-1.2	1.42
0.7	0.586	0.574	0.56	-2	-2.4	0.84
0.8	0.626	0.607	0.584	-3.1	-3.6	0.86
0.9	0.626	0.596	0.559	-4.8	-5.8	0.83
1	0.54	0.497	0.45	-7.9	-8.8	0.9
Ave.				2.8	2.6	

As shown in Tables 6–8, the differences between the solution values (s_1 , s_2 , and s_3) obtained from G1, G2, and G3 exhibit oscillatory convergence, which is reflected in the ratios $R = \varepsilon_{12}/\varepsilon_{23}$. Consequently, Richardson extrapolation does not provide reliable uncertainty estimates in many cases.

In the pump-jet propulsive system, deriving the regression formula for POW between the conventional advance coefficient J and the propeller hydrodynamic properties, without additionally measuring the flow velocity at the duct inlet, leads to difficulties in body-force implementation. This is because the propeller inflow plane, which is typically prescribed at the propeller inlet, exhibits a flow velocity that increases significantly compared to the hull-relative velocity when a duct is present.

To address this, an additional regression relation is introduced between the hull-relative advance coefficient J and the duct-inlet advance coefficient J_A . Accordingly, the regression formula for the propeller hydrodynamic properties is expressed in terms of J_A rather than J . The computation of J_A is performed at the inflow plane shown previously in Figure 5, and the relation between J and J_A is presented in Figure 10 and Table 9. In Equation (5a), the values of J_1 and J_0 are set to 0.5123 and 0.5096, respectively. The resulting variations in the POW coefficients are summarized in Tables 10 and 11. The effect of the grid resolution on the computed J_A values is found to be negligible, as visually demonstrated in Figure 11.

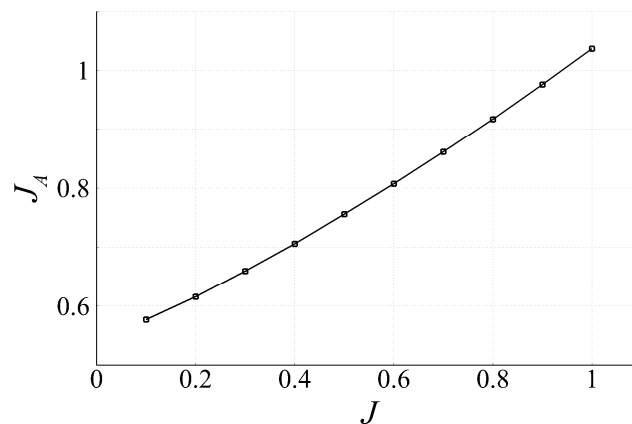


Figure 10. Correlation between J and J_A achieved from POW simulations using G2 DP model.

Table 9. J , J_A , u , and u_A values measured from POW simulations using G2 DP model.

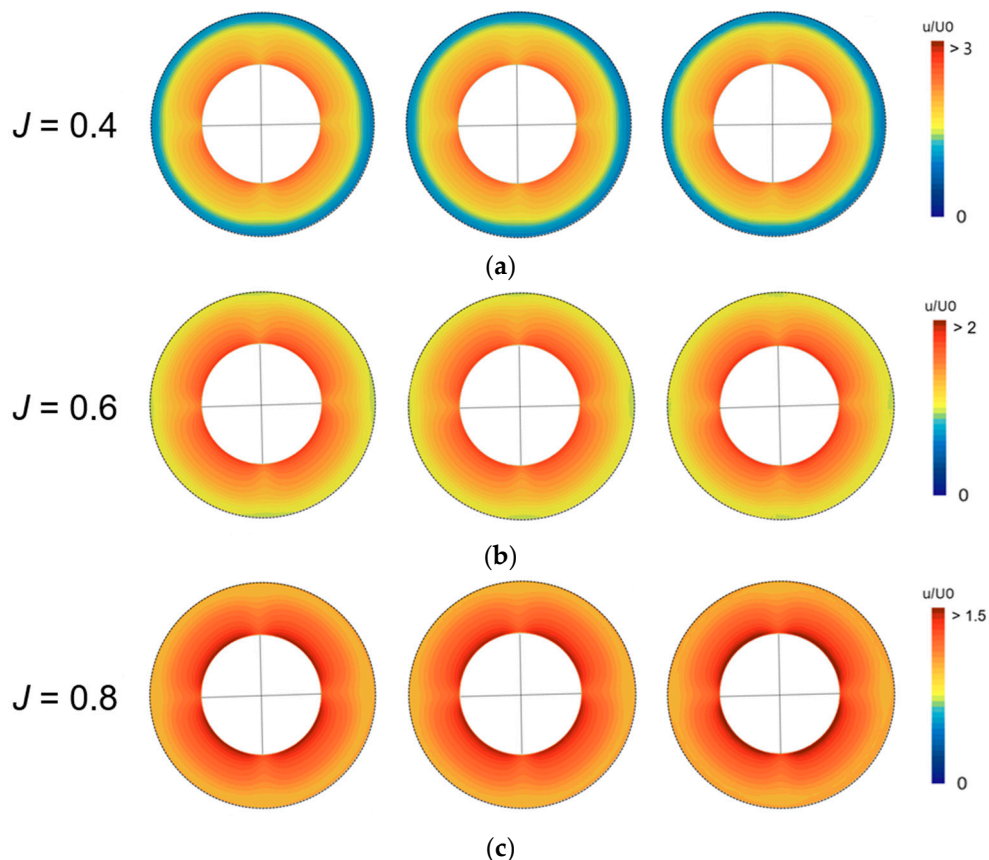
J	u	u_A	J_A
0.1	0.255	1.472	0.577
0.2	0.510	1.571	0.616
0.3	0.765	1.684	0.660
0.4	1.020	1.802	0.706
0.5	1.275	1.927	0.756
0.6	1.530	2.059	0.807
0.7	1.785	2.195	0.861
0.8	2.040	2.339	0.917
0.9	2.295	2.488	0.976
1.0	2.550	2.644	1.037

Table 10. Coefficients of POW characteristics regression curve built upon J .

Coefficient	Value	Coefficient	Value
K_{T0}	0.3582	K_{Q0}	0.0582
K_{T1}	-0.1993	K_{Q1}	-0.0256
K_{T2}	-0.0937	K_{Q2}	-0.0128

Table 11. Coefficients of POW characteristics regression curve built upon J_A .

Coefficient	Value	Coefficient	Value
K_{T0}	0.6187	K_{Q0}	0.0919
K_{T1}	−0.4329	K_{Q1}	−0.0551
K_{T2}	−0.0981	K_{Q2}	−0.0140

**Figure 11.** Grid triplet's axial inflow speed distribution at duct inlet (left: G1, middle: G2, right: G3): (a) $J = 0.4$; (b) $J = 0.6$; (c) $J = 0.8$.

The body-force modeling is carried out using the POW regression formula based on J_A , and validation against the discretized propeller is performed through POW simulations. Figure 12 presents a comparison of the hydrodynamic properties. For thrust, the body-force model shows an overestimation in the region of $J < 0.5$, although the overall accuracy remains reasonable. In the case of torque, the body-force model generally exhibits overestimation. This behavior appears unrelated to the accuracy of J_A measured for the discretized and body-force propellers, as shown in Figure 12d. Instead, it is considered to result from the interaction between the duct and the modified pressure field induced by the body-force propeller.

Since this issue is also related to grid resolution, the present study proceeds without further debugging to maintain a practical approach. Ultimately, torque does not influence the 3DOF simulations, and therefore, no additional corrective measures are taken. Body-force modeling is not only important for predicting thrust but also for reproducing the flow field around the hull with sufficient fidelity, particularly because the rudder and propulsion system are usually placed in close proximity. As confirmed by representative advance coefficients, the body-force model predicts a velocity distribution similar to that of the discretized propeller (Figure 13).

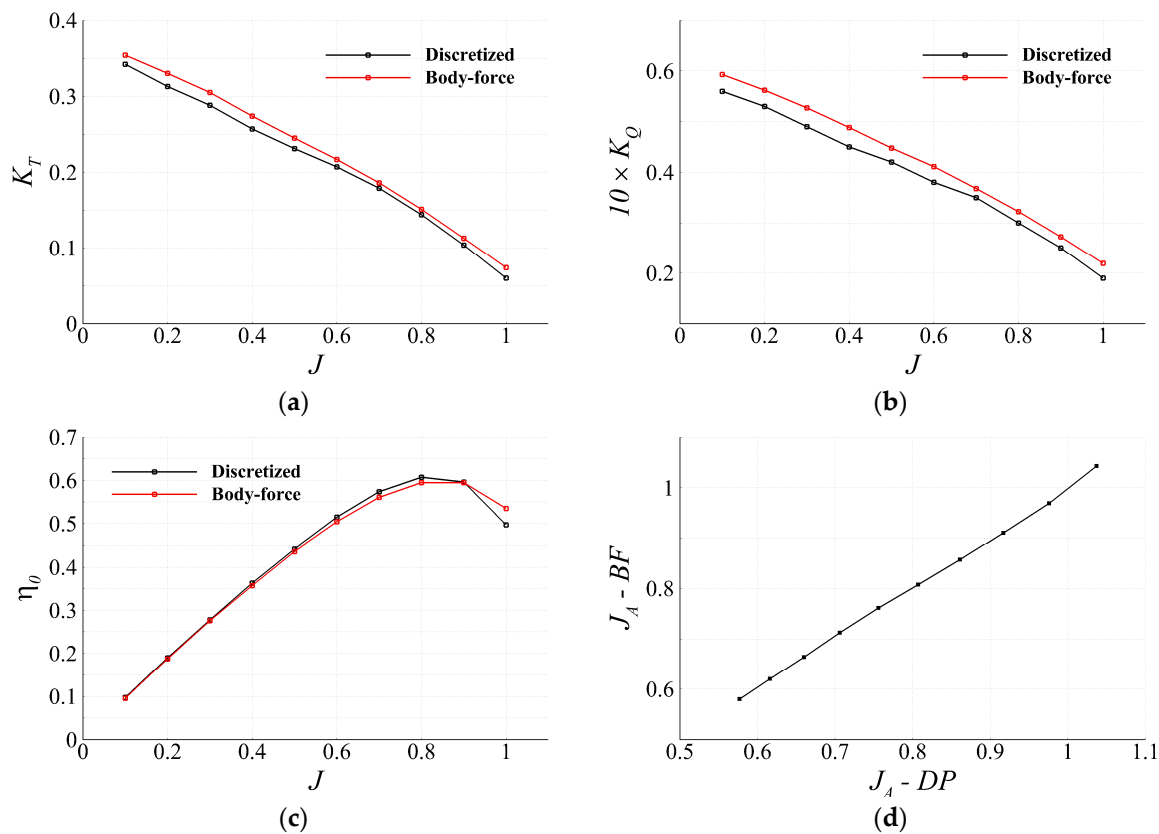


Figure 12. Validation of CFD BF model against DP model: (a) thrust coefficient; (b) torque coefficient; (c) propeller open-water efficiency; (d) advance coefficient at duct inlet.

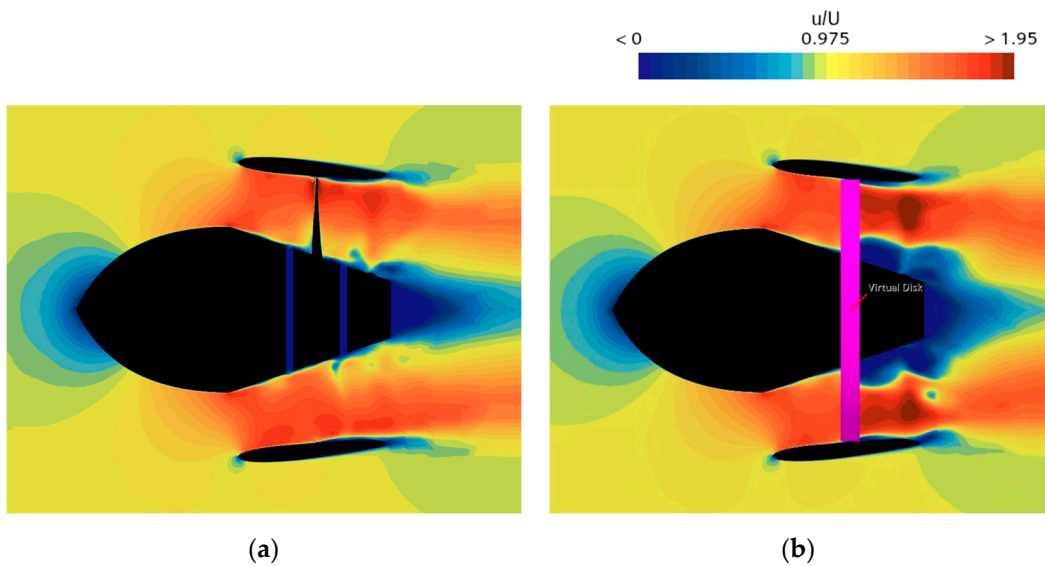


Figure 13. Axial inflow speed distribution near the propulsion system: (a) DP model; (b) BF model.

5.3. Resistance Test

The resistance test (Figure 14) focuses primarily on constructing Equation (11) and performing CFD data verification for the AUV hull and rudders using the grid triplet.

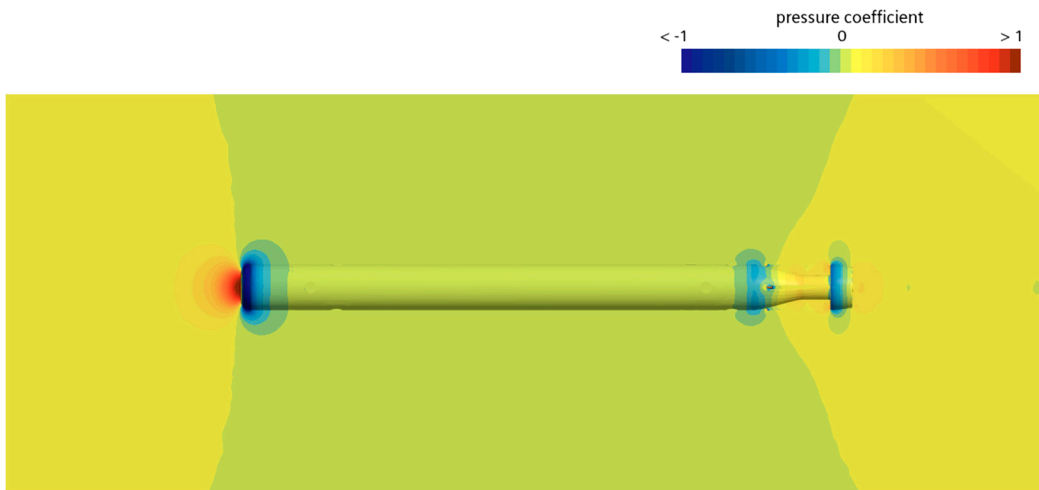


Figure 14. Pressure distribution at the steady state of resistance simulation.

In this setup, the duct is included, while the propeller is excluded to enable replacement with the body-force model. The simulation results are presented in Figure 15. In addition, the measured frictional resistance during straight-ahead motion of the AUV shows close agreement with the ITTC 1957 regression formula (frictional resistance coefficient, $C_F = 0.075/(\log(Rn) - 2)^2$) commonly used for ships. This suggests that if pressure-field regression is carried out for an AUV digital twin, the frictional resistance can be modeled as a major feature through a simple regression expression.

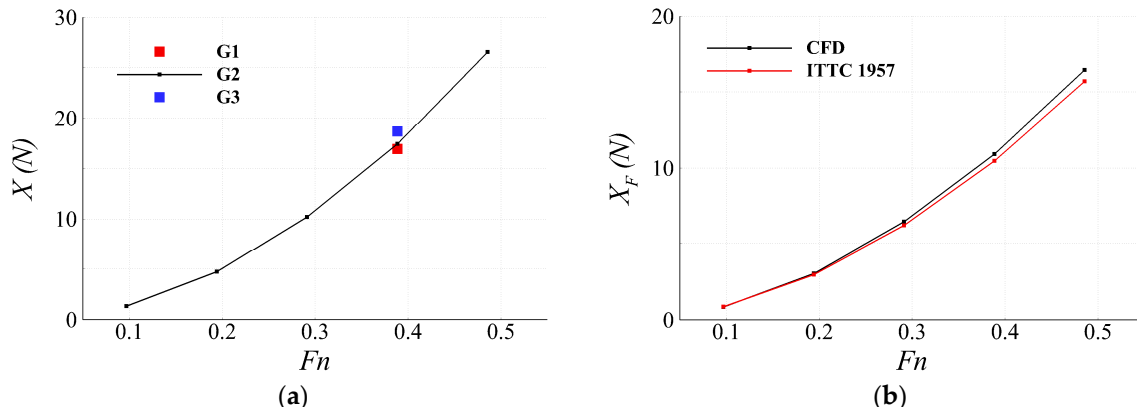


Figure 15. Resistance test results: (a) resistance curve against Froude number; (b) frictional resistance curve against Froude number.

The coefficients applied in Equation (11) are listed in Table 12. Furthermore, the grid dependency of the axial flow speed at the duct inlet, expressed as J_A , is examined (Figure 16). Qualitatively, it is confirmed that the G2 resolution yields results nearly identical to those of the G1 grid. Similar to the POW case, the G2 grid, which represents the median resolution, was chosen for the remainder of the simulations.

Table 12. Coefficients of resistance regression curve (Figure 15a).

Coefficient	Value
R_0	-0.2792
R_1	6.5738
R_2	100.212

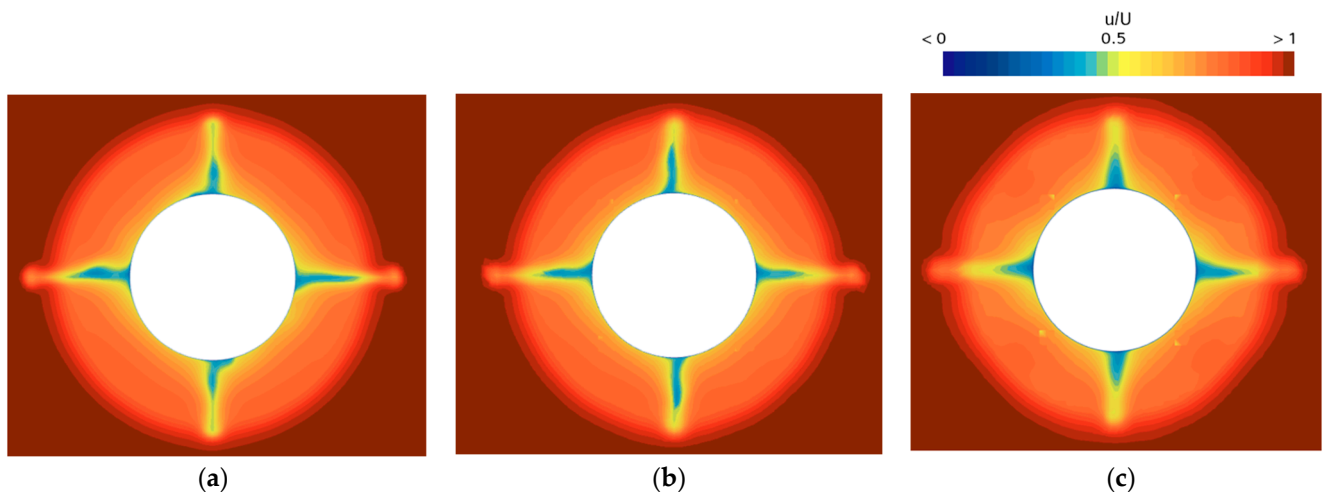


Figure 16. Grid triplet's axial inflow speed at the duct inlet during resistance simulation: (a) G1; (b) G2; (c) G3.

Figure 17 presents the $y+$ distribution calculated from the resistance test using the grid triplet. Considering that the hull wake reduces axial velocity, the rudder and propulsion regions consistently exhibit lower $y+$ values than the hull, also indicating that the height of the first grid cell off the wall is fairly uniform. As a result, achieving a uniform $y+$ distribution over the entire AUV body is difficult, and computation therefore relies on the “all $y+$ wall treatment” for practical use. Since the G2 grid system is adopted for the remainder of the CFD simulations, its $y+$ distribution is examined in detail, while those of G1 and G3 are proportionally decreased or increased relative to G2.

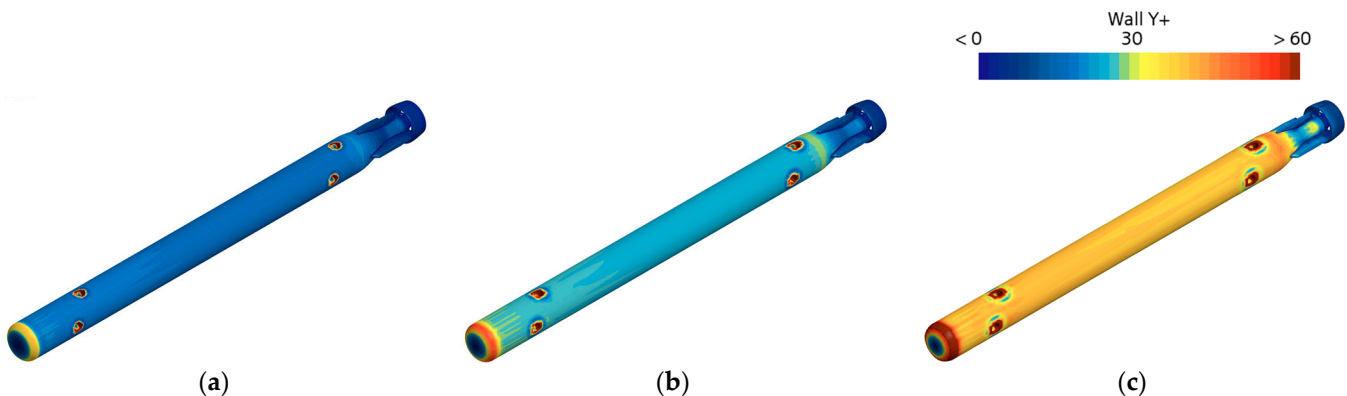


Figure 17. $y+$ distribution of the grid triplet: (a) G1; (b) G2; (c) G3.

Ideally, wall shear stress and the resulting crossflow are most accurately resolved when $y+$ resides either in the viscous sublayer ($y+ < 1$) or in the log-law region ($y+ > 30$). The G2 grid, however, falls within the buffer layer ($1 < y+ < 30$). Thus, although the first cell height in the main body region is relatively small, the blended wall function combining the viscous sublayer and log-law formulations is applied, which may introduce inaccuracies in crossflow prediction and leaves room for further improvement. Nevertheless, the grid triplet produces nearly identical propeller inflow (Figure 15) and comparable shear stress between G1 and G2, thereby offering a practical trade-off between computational cost and accuracy.

5.4. Self-Propulsion Test

In the self-propulsion test (Figure 18), body-force propulsion is implemented, and the simulation is carried out in 1DOF. At the target Froude number, the propeller rotational speed n , the value of ω_0 used in Equation (8b), and the value of t_p used in Equation (12a) are determined through adjustment during the simulation. As shown in Figure 19a, three cases using different n are tested, and the final n is determined at the point where the longitudinal force coefficient X' becomes zero. The propeller RPS obtained from CFD is directly applied in subsequent free-running simulations.

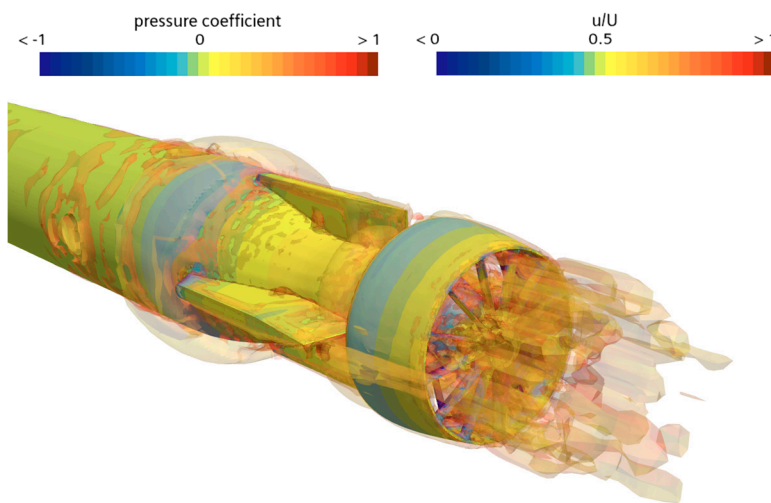


Figure 18. Pressure distribution and propeller wake ($Q = 10$) during self-propulsion simulation. (Colored contours on the hull surface and vortex core indicate pressure coefficient and axial velocity, respectively.)

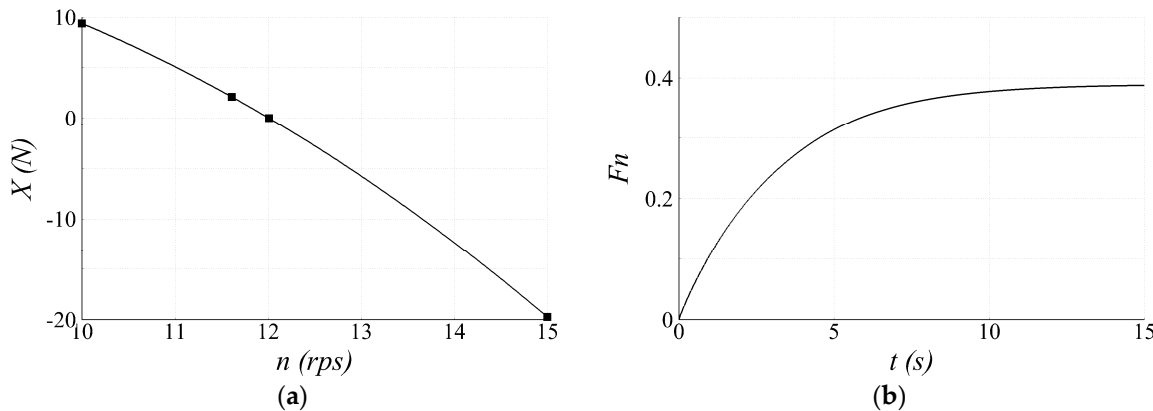


Figure 19. Self-propulsion simulation results at target Froude number: (a) propeller rotational speed tested for finding self-propulsion point; (b) time history of ship speed represented as instantaneous Froude number during self-propulsion simulation using zero initial ship speed and propeller rotational speed found at self-propulsion point.

The values of ω_0 and t_p , however, are determined differently. First, the surrogate expressions required for the self-propulsion test (Equations (5), (8), (9), (11), and (12a)) are constructed. Then, by executing the surrogate and adjusting ω_0 and t_p , values of K_T , X' , and X_P' comparable to those from CFD are identified. The final adjusted ω_0 and t_p values are 0.233 and 0.13, respectively.

5.5. Static Drift and Control Fin Tests

In the static drift test (Figure 20a), the maneuvering coefficients associated with lateral velocity v are identified, while in the control-fin test (Figure 20b), the maneuvering coefficients associated with the vertical rudder angle δ are determined. The coefficients are the result of using the least-squares (LSQ) method functionality in Matlab. Equation (14) presents the use of the matrix setup when obtaining the maneuvering coefficients for sway force using LSQ.

$$\begin{bmatrix} | \\ Y' \\ | \end{bmatrix} = \begin{bmatrix} | & & | \\ v' & v'|v'| & v'v'v' \\ | & | & | \end{bmatrix} \begin{bmatrix} Y_v \\ Y_{v|v|} \\ Y_{vvv} \end{bmatrix} \quad (14)$$

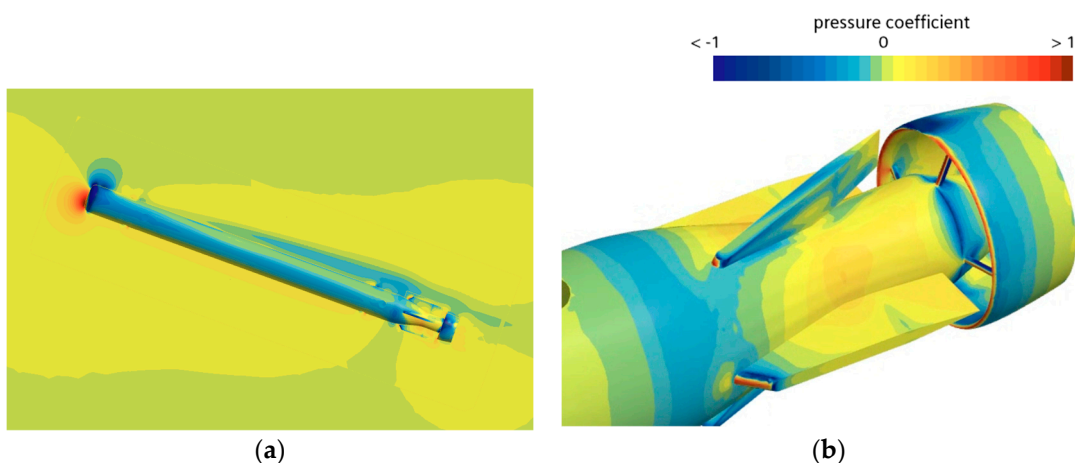


Figure 20. Pressure distributions: (a) static drift ($\beta = 20^\circ$); (b) control fin simulation ($\delta = 20^\circ$).

The reconstructed forces and moments based on the fitted coefficients are presented in Figure 21. The coefficients applied in surrogate Equation (12) are summarized in Tables 13 and 14.

Table 13. Coefficients of regression curves achieved from static drift simulations.

Coefficient	Value	Coefficient	Value	Coefficient	Value
X_{vv}	0.1574	Y_v	-0.1686	N_v	0.0331
X_{vvvv}	-1.9794	$Y_{v v }$	0.2658	$N_{v v }$	0.0616
X_{vvvvvv}	7.7387	Y_{vvv}	-2.2175	N_{vvv}	-0.4145

Table 14. Coefficients of regression curves achieved from control fin simulations.

Coefficient	Value	Coefficient	Value	Coefficient	Value
$X_{ \delta }$	-0.0018	Y_δ	-0.0094	N_δ	-0.0023
$X_{\delta\delta}$	0.0294	$Y_{\delta \delta }$	-0.0245	$N_{\delta \delta }$	-0.0093
		$Y_{\delta\delta\delta}$	-0.0082	$N_{\delta\delta\delta}$	-0.0069

5.6. Pure Sway and Pure Yaw Tests

In the pure sway test, the maneuvering coefficients associated with lateral acceleration \dot{v} are obtained, while in the pure yaw test, the coefficients associated with yaw rate r and yaw acceleration \dot{r} are identified. As introduced in the test matrix (Table 5), the pure sway test is conducted by imposing a sinusoidal sway motion at the target Froude number, and the pure yaw test is performed by superimposing a sinusoidal yaw motion (Figure 22a,d). The resulting forces and moments during pure sway are presented in Figure 22b,c, while those during pure yaw are shown in Figure 22e,f.

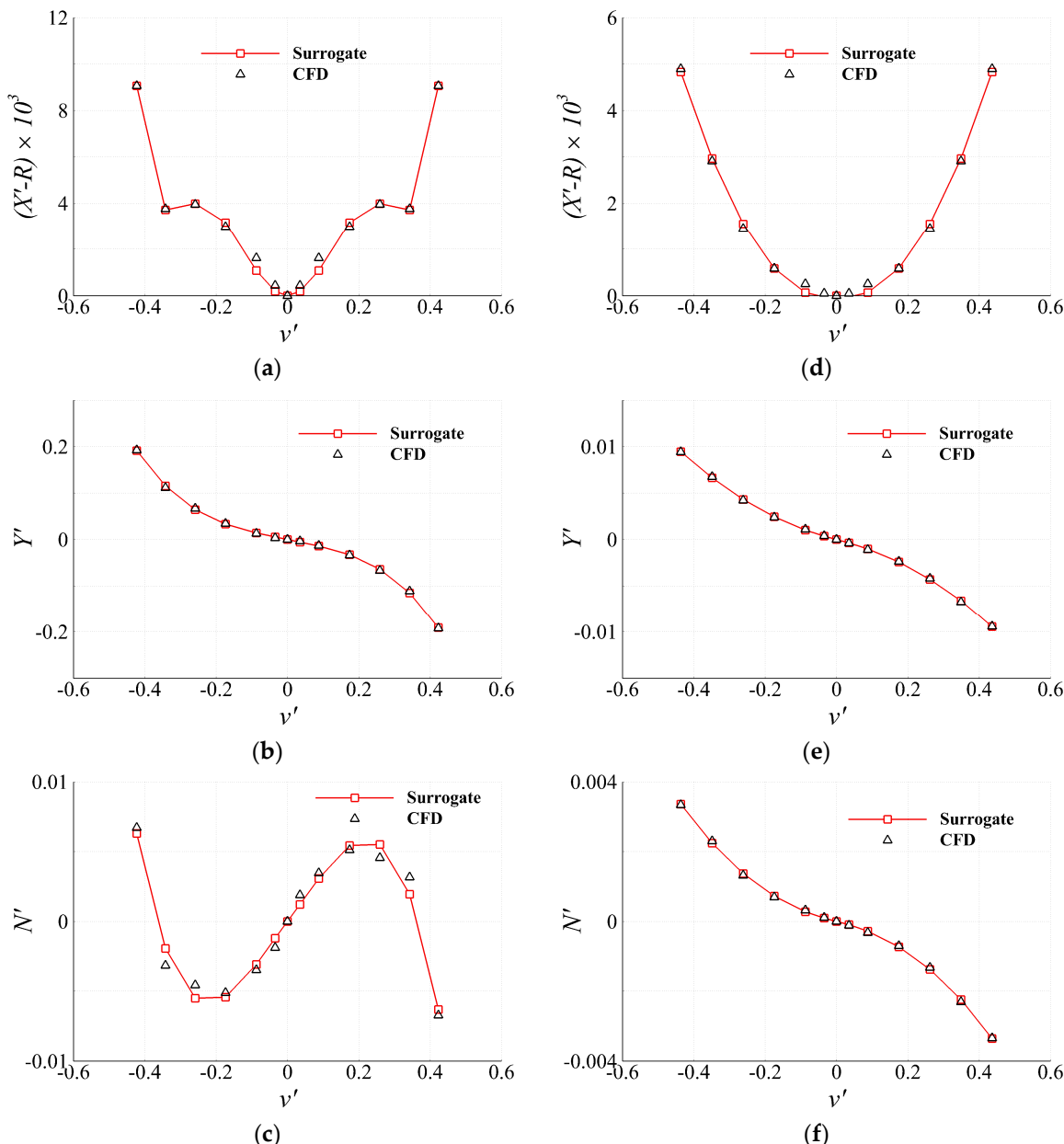


Figure 21. Measured forces and moment and regression curve for surrogate in static drift simulations: (a) surge force; (b) sway force; (c) yaw moment, and control fin simulation: (d) surge force; (e) sway force; (f) yaw moment.

In the pure sway test, the velocity-dependent forces and moments (Y'_{VEL} , N'_{VEL}) are subtracted from the measured total force and moment (Y' , N'), respectively, using the surrogate regression expressions obtained from the static drift test, and the acceleration-dependent terms (Y'_{ACC} , N'_{ACC}) are identified through the least-squares method (Table 15). In the pure yaw test, both the velocity-dependent and acceleration-dependent forces and moments are simultaneously determined using the least-squares method (Table 16).

Table 15. Coefficients of regression curves achieved in pure sway simulations.

Coefficient	Value	Coefficient	Value
Y_v	-0.129	N_v	-0.0088

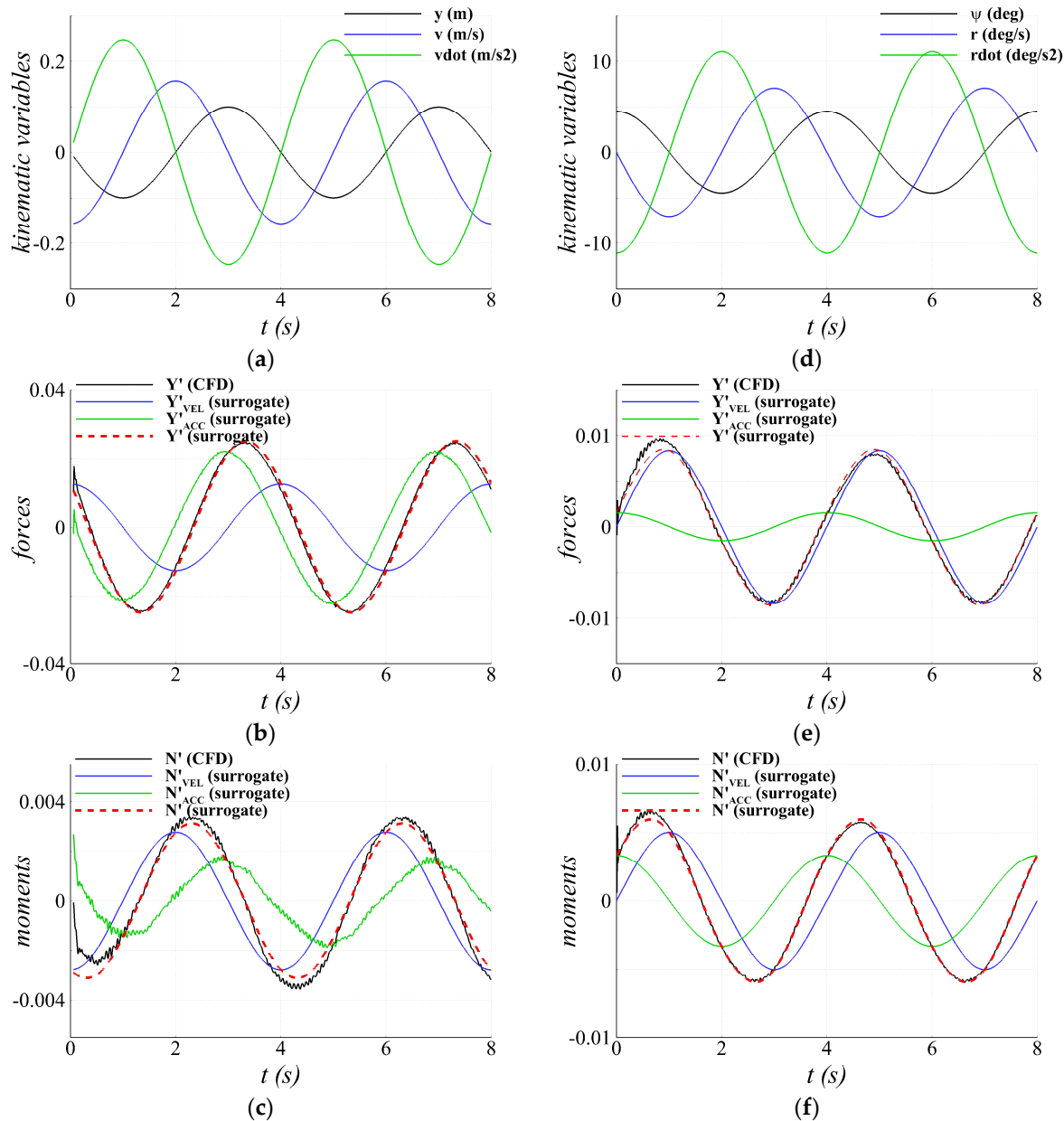


Figure 22. The measured time histories: (a) sway displacement, velocity, and acceleration from both pure sway and pure yaw; (b) sway force from pure sway; (c) yaw moment from pure sway; (d) yaw displacement, velocity, and acceleration from pure yaw; (e) sway force from pure yaw; (f) yaw moment from pure yaw.

Table 16. Coefficients of regression curves achieved in pure yaw simulations.

Coefficient	Value	Coefficient	Value
Y_r	-0.04458	N_r	-0.02690
$Y_{r r }$	-0.03431	$N_{r r }$	-0.01989
$Y_{\dot{r}}$	-0.00432	$N_{\dot{r}}$	-0.00944

5.7. Forced Oscillation

In the forced oscillation test, the AUV is subjected to a sinusoidal sway motion at $Fn = 0$ to determine the added mass coefficient m_y (Figure 23). To obtain m_y , the simulation

is briefly modeled assuming that the measured force is the sum of force affected by damping and inertia, which are assumed to be proportional to velocity and acceleration as follows:

$$m_y \ddot{y} + b\dot{y} = Y \quad (15)$$

where b denotes the damping coefficient. Since the acceleration term exhibits sine function behavior, the side force is convoluted with the same sine function sharing the same frequency to obtain m_y . The coefficient m_x is found to be negligible in the results and is therefore not reported. Since added mass does not vary significantly, the period and amplitude of the sinusoidal input are selected to represent the typical operating range of the AUV. The non-dimensionalized added moment of inertia in z-direction 0.009 from [33] is directly used for the estimation of dimensional value (J_z). A more accurate estimation of the AUV's J_z would require a forced oscillation test in yaw.

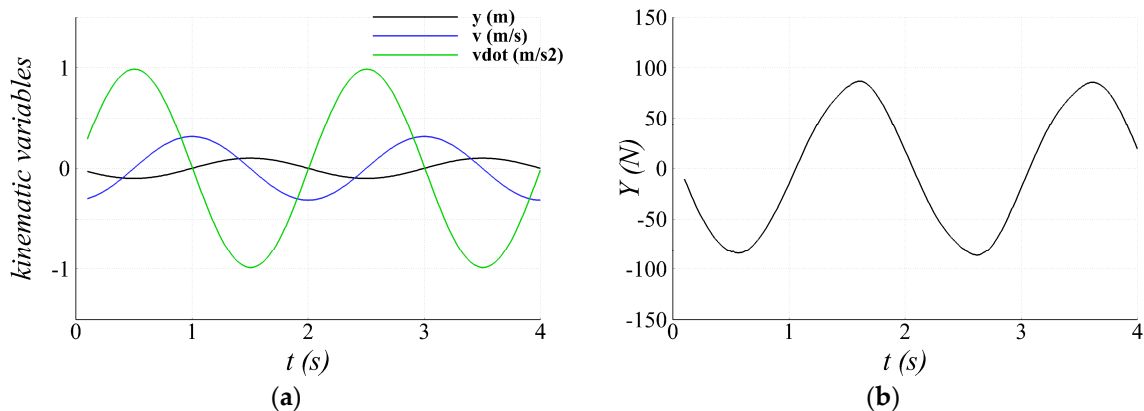


Figure 23. The measured time histories during forced oscillation simulation: (a) sway displacement, velocity, and acceleration; (b) sway force.

6. Assessment of Free-Running Capability

The complete form of the surrogate is utilized to predict free-running performance for 1DOF self-propulsion and 3DOF zigzag +20/20 simulations, and the predictions are validated against the corresponding CFD results. The validation is carried out with respect to the kinematic variables, J_A , and the forces and moments. The result demonstrates good agreement, confirming the surrogate's ability to reproduce the dominant maneuvering characteristics within the tested conditions.

6.1. 1DOF Self-Propulsion

The initial ship velocity is set to zero, with the propeller rotation speed fixed at the value obtained from the CFD self-propulsion simulation. In this setup, the primary considerations are the regression curve for resistance, the regression curve for propeller thrust, and the empirical values of thrust deduction and wake fraction.

The surrogate successfully predicts the transitional characteristics of surge velocity during acceleration, as well as the attenuation of the total surge force, in good agreement with the CFD results (Figure 24). This indicates the surrogate's capability to mimic CFD behavior within the Froude number regime lower than the target value.

However, discrepancies remain in the transition region. The major sources of mismatch are expected to be (1) the use of a uniform thrust deduction and (2) the use of a uniform wake fraction, both of which would require additional data for improved regression. Nevertheless, the steady-state values match closely, suggesting that the surrogate

is sufficiently reliable for maneuvering simulations initiated from the steady-state self-propulsion condition.

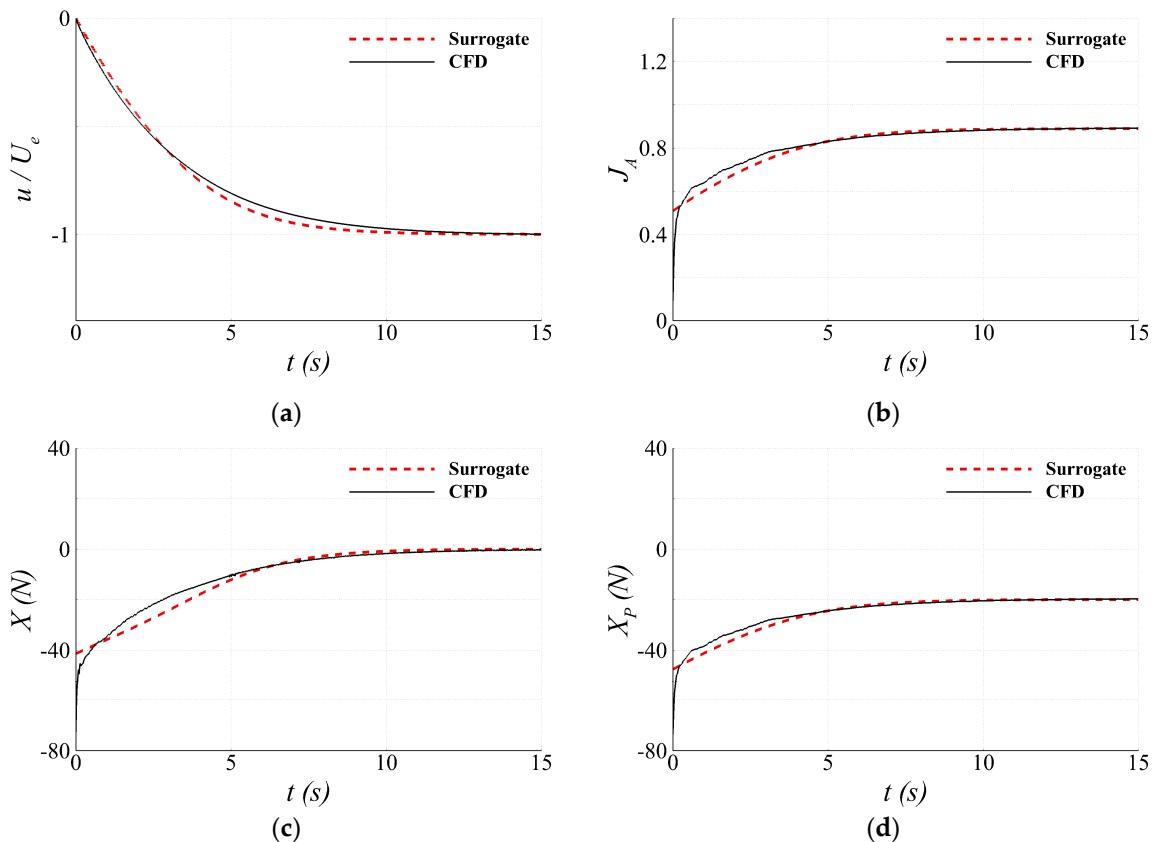


Figure 24. Time histories during 1DOF free-running self-propulsion simulations: (a) surge velocity; (b) advance coefficient at the duct inlet; (c) total surge force; (d) propeller thrust.

6.2. 3DOF Zigzag +20/20

The rudder controller for the zigzag +20/20 maneuver is activated in both the CFD and surrogate simulations once the 1DOF self-propulsion condition reaches a steady state and the 3DOF motions are released.

As shown in Figure 25, the surrogate continues to reproduce the overall motion period with reasonable accuracy even beyond the second overshoot, occurring near $t = 25$ s. Although the velocity components are occasionally overpredicted, this does not affect the oscillation period. The surrogate also captures the decreasing trend of the advance coefficient immediately prior to the onset of turning. While the drift angle tends to be overpredicted at both low and high peaks, the level of overestimation does not result in an unrealistic trajectory caused by excessive propulsion.

The comparison of forces and moments in Figure 26 provides further support. The propeller thrust follows the same trend as the advance coefficient, producing lower thrust under conditions of a high advance coefficient. The total surge force, directly correlated with both the advance coefficient and propeller thrust, shifts to lower values than CFD. However, the surge velocity itself shows little change, suggesting that the mean surge velocity is primarily governed by the resistance coefficient, while only the fluctuations are influenced by sway or yaw velocity. This reduces the importance of Equation (12a) apart from the resistance term.

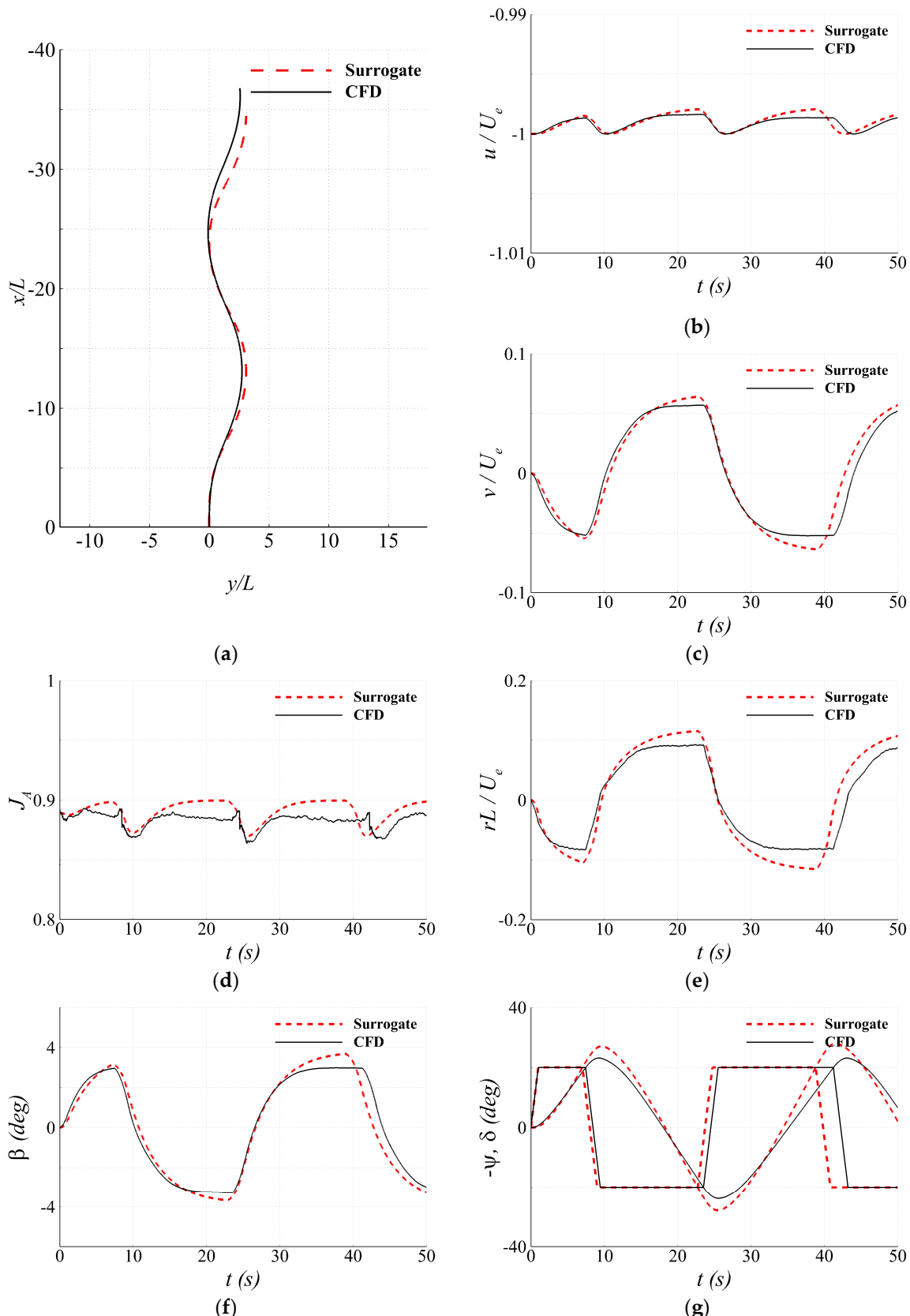


Figure 25. Time histories of kinematic variables and advance coefficient at the duct inlet during free-running zigzag simulations: (a) trajectory; (b) surge velocity; (c) sway velocity; (d) advance coefficient at the duct inlet; (e) yaw velocity; (f) drift angle; (g) yaw and rudder angles.

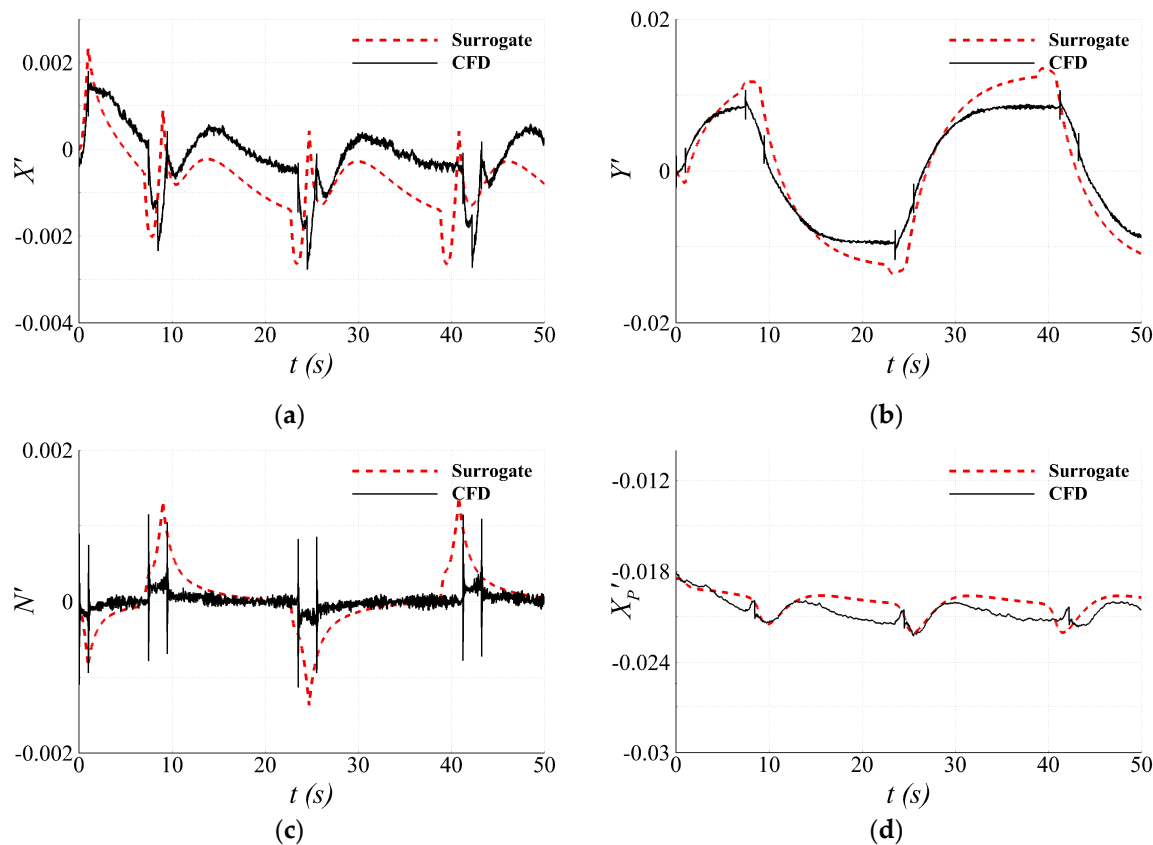


Figure 26. Time histories of forces and moment during free-running zigzag simulations: (a) total surge force; (b) total sway force; (c) total yaw moment; (d) propeller thrust.

The side force Y' and yaw moment N' rise sharply just before turning. The yaw moment exhibits a suppressed response in CFD but a more pronounced pulse in the surrogate. This discrepancy originates from Equations (10a,b) and (12b,c), since propulsion only contributes to surge force. Equation (12b,c) are directly obtained from CFD by assuming quasi-static behavior in free-running snapshots, with Equation (10a,b) used to supplement conditions involving both the drift angle and rudder angle, thereby reducing the data acquisition requirement. Introducing the drift angle through Equation (10b) appears acceptable, as CFD results show a strong correlation between sway force and drift angle. The yaw moment, however, is more step-like, following the rudder signal and showing a weaker correlation with the drift angle, which implies that Equation (10b) requires further refinement with reduced influence of the drift angle and a more pronounced role of rudder angle for moment estimation.

Nevertheless, the sudden spike in yaw moment predicted by the surrogate is temporary and recovers quickly, indicating that the turning moment is proportionally small relative to the steady-turning region. Overall, the surrogate reproduces the key features of the turning behavior observed in CFD while leaving room for further improvement.

7. Conclusions

In this study, a surrogate model for AUV maneuvering is established using CFD, and its accuracy is assessed. The pump-jet propulsion system is modeled both to reduce the CFD computation time and to enable implementation in the surrogate. The required CFD simulations are further minimized by employing kinematic formulations for the hull rudder force and moment modules, while the surrogate is analytically constructed through additional kinematic relations and a limited set of empirical parameters, i.e., thrust deduction

and wake fraction. The overall surrogate framework is expected to yield consistent results as long as the variations in model length remain limited. While the surrogate is constructed under the Froude number 0.39 condition for side force, the resistance curve, which is the most sensitive factor to Froude number, is obtained at several points and regressed to cover a range of forward speeds. Since the side force is scaled and its coefficients do not significantly deviate with respect to forward speed, the framework is expected to remain valid, pending further validation.

At the preliminary design stage, CFD proves to be valuable not only for predicting the flow field but also for reproducing diverse scenarios through integration with controllers and propeller models. This reaffirms the advantage of predicting physical data directly from geometric information. Nevertheless, the intrinsic limitation of high computational cost remains. Therefore, as a CFD-derived next step, the present surrogate approach is expected to serve as a reduced-order model for hydrodynamic force prediction, particularly when coupled with control models or employed as training data for a multivariate system identification framework. In this role, it enables long-horizon maneuvering simulations, including full kinematics and trajectory, within minutes (e.g., predefined waypoint tracking).

The principal limitation of the present surrogate is generic to most surrogates: any geometric change requires re-obtaining regression data and re-identifying the coefficients. In addition, ambient current during AUV operation modifies the reduced-order model; even for a data-driven approach, the current acts as an exogenous input and requires additional sensing (e.g., water-relative velocity or current estimates) to avoid bias. While more advanced modules can be integrated, the current surrogate is suitable for early-stage design and control studies. It is anticipated that this framework can serve as a backbone for future developments, such as more advanced rudder models, propeller models incorporating side-force effects [34], full 6DOF extensions, and explicit current modeling. In the free-running simulations, it is also observed that the rudders of the current AUV design are relatively small, resulting in limited lifting force and confining zigzag motions to small values of drift angle. This finding implies the need for further surrogate validation at larger drift angles, particularly when side thruster models are incorporated.

Author Contributions: Conceptualization, D.-H.K., J.S., and H.C.; methodology, D.-H.K. and J.S.; software, Y.K.; validation, Y.K. and D.-H.K.; formal analysis, Y.K. and D.-H.K.; investigation, Y.K. and D.-H.K.; resources, J.S. and H.C.; data curation, D.-H.K.; writing—original draft preparation, Y.K.; writing—review and editing, D.-H.K.; visualization, Y.K. and D.-H.K.; supervision, D.-H.K.; project administration, H.C.; funding acquisition, H.C. All authors have read and agreed to the published version of the manuscript.

Funding: This research was supported by the Challengeable Future Defense Technology Research and Development Program through the Agency for Defense Development (ADD), funded by the Defense Acquisition Program Administration (DAPA) in 2025 (No. 915071101).

Data Availability Statement: The data presented in this study are available upon request from the corresponding author.

Conflicts of Interest: The authors declare no conflicts of interest.

References

1. Caccia, M.; Bibuli, M.; Bono, R.; Bruzzone, G. Basic navigation, guidance and control of an Unmanned Surface Vehicle. *Auton. Robot.* **2008**, *25*, 349–365. [[CrossRef](#)]
2. Bellingham, J.G.; Rajan, K. Robotics in remote and hostile environments. *Science* **2007**, *318*, 1098–1102. [[CrossRef](#)]
3. Griffiths, G. (Ed.) *Technology and Applications of Autonomous Underwater Vehicles*; CRC Press: Boca Raton, FL, USA, 2002; pp. 335–358.

4. Woolsey, C.A.; Leonard, N.E. Stabilizing underwater vehicle motion using internal rotors. *Automatica* **2002**, *38*, 2053–2062. [\[CrossRef\]](#)
5. Wang, X.; Shang, J.; Luo, Z.; Tang, L.; Zhang, X.; Li, J. Reviews of power systems and environmental energy conversion for unmanned underwater vehicles. *Renew. Sustain. Energy Rev.* **2012**, *16*, 1958–1970. [\[CrossRef\]](#)
6. Hasvold, Ø.; Størkersen, N.J.; Forseth, S.; Lian, T. Power sources for autonomous underwater vehicles. *J. Power Sources* **2006**, *162*, 935–942. [\[CrossRef\]](#)
7. Tan, Y.; Zheng, Z.-Y. Research Advance in Swarm Robotics. *Def. Technol.* **2013**, *9*, 18–39. [\[CrossRef\]](#)
8. Wynn, R.B.; Huvenne, V.A.I.; Le Bas, T.P.; Murton, B.J.; Connally, D.P.; Bett, B.J.; Ruhl, H.A.; Morris, K.J.; Peakall, J.; Parsons, D.R.; et al. Autonomous Underwater Vehicles (AUVs): Their past, present and future contributions to the advancement of marine geoscience. *J. Mar. Geol.* **2014**, *352*, 451–468. [\[CrossRef\]](#)
9. Liu, J.; Yu, F.; Yan, T.; He, B. Self-propulsion performance predictions of AUV based on response surface methodology. *Ocean Eng.* **2023**, *287*, 115923. [\[CrossRef\]](#)
10. Hammond, B.; Sapsis, T.P. Reduced order modeling of hydrodynamic interactions between a submarine and unmanned underwater vehicle using non-myopic multi-fidelity active learning. *Ocean Eng.* **2023**, *288*, 116016. [\[CrossRef\]](#)
11. Fan, G.; Liu, X.; Hao, Y.; Yin, G.; He, L. Optimized Hydrodynamic Design for Autonomous Underwater Vehicles. *Machines* **2025**, *13*, 194. [\[CrossRef\]](#)
12. Wang, Y. Rapid Data-Driven Individualized Shape Design of AUVs. *SSRN* **2023**. *preprint*. [\[CrossRef\]](#)
13. Yoerger, D.R.; Jakuba, M.; Bradley, A.M.; Bingham, B. Techniques for deep sea near bottom survey using an autonomous underwater vehicle. *Int. J. Robot. Res.* **2007**, *26*, 41–54. [\[CrossRef\]](#)
14. Camilli, R.; Reddy, C.M.; Yoerger, D.R.; Van Mooy, B.A.S.; Jakuba, M.V.; Kinsey, J.C.; McIntyre, C.P.; Sylva, S.P.; Maloney, J.V. Tracking hydrocarbon plume transport and biodegradation at Deepwater Horizon. *Science* **2010**, *330*, 201–204. [\[CrossRef\]](#)
15. Liu, X.; Ji, X.; Lei, L. Surrogate-based drag optimization of Autonomous Remotely Vehicle using an improved Sequentially Constrained Monte Carlo Method. *Ocean Eng.* **2024**, *297*, 117047. [\[CrossRef\]](#)
16. Vardhan, H.; Hyde, D.; Timalsina, U.; Volgyesi, P.; Sztipanovits, J. Sample-Efficient and Surrogate-Based Design Optimization of Underwater Vehicle Hulls. *arXiv* **2023**, arXiv:2304.12420. [\[CrossRef\]](#)
17. Li, C.-S.; Wang, P.; Qiu, Z.-M.; Dong, H.-C. A Double-Stage Surrogate-Based Shape Optimization Strategy for Blended-Wing-Body Underwater Gliders. *China Ocean Eng.* **2020**, *34*, 400–410. [\[CrossRef\]](#)
18. Lin, Y.-H.; Chiu, Y.-C. The estimation of hydrodynamic coefficients of an autonomous underwater vehicle by comparing a dynamic mesh model with a horizontal planar motion mechanism experiment. *Ocean Eng.* **2022**, *249*, 110847. [\[CrossRef\]](#)
19. Safari, F.; Rafeeyan, M.; Danesh, M. Estimation of hydrodynamic coefficients and simplification of the depth model of an AUV using CFD and sensitivity analysis. *Ocean Eng.* **2022**, *263*, 112369. [\[CrossRef\]](#)
20. Miller, L.M.; Brizzolara, S. Effect of amplitudes and frequencies on Virtual Planar Motion Mechanism of AUVs, Part I: Forces, moments and hydrodynamic derivatives. *Ocean Eng.* **2023**, *286*, 115512. [\[CrossRef\]](#)
21. Miller, L.M.; Krauss, S.; Brizzolara, S.; Gilbert, C.; Stilwell, D. Effect of amplitudes and frequencies on Virtual Planar Motion Mechanism of AUVs: Part II 3DOF implementation, comparison with RANSE and field trials. *Ocean Eng.* **2023**, *289*, 116242. [\[CrossRef\]](#)
22. Cai, B.; Mao, X.; Xu, Q.; Chai, W.; Tian, B.; Qiu, L. Simulation of the interaction between ship and ducted propeller with a modified body force method. *Ocean Eng.* **2022**, *249*, 110950. [\[CrossRef\]](#)
23. Wang, H.; Xiang, X.; Xiang, G.; Liu, C.; Yang, L. An improved body force method for simulation of self-propulsion AUV with ducted propeller. *Ocean Eng.* **2023**, *281*, 114731. [\[CrossRef\]](#)
24. Mentor, F.R. Two-Equation Eddy-Viscosity Turbulence Models for Engineering Applications. *AIAA J.* **1994**, *32*, 1598–1605. [\[CrossRef\]](#)
25. Salari, M.; Rava, A. Numerical investigation of hydrodynamic flow over an AUV moving in the water-surface vicinity considering the laminar-turbulent transition. *J. Mar. Sci. Appl.* **2017**, *16*, 298–304. [\[CrossRef\]](#)
26. Liu, B.; Yin, Z.; An, Q.; Zhang, X. Boundary-layer transition on a shallowly submerged vehicle. *Ocean Eng.* **2025**, *317*, 120051. [\[CrossRef\]](#)
27. Liu, B.; Vanierschot, M.; Buysschaert, F. Comparison Study of the $k - k L - \omega$ and $\gamma - Re\theta$ Transition Model in the Open-Water Performance Prediction of a Rim-Driven Thruster. *Int. J. Turbomach. Propuls. Power* **2024**, *9*, 2. [\[CrossRef\]](#)
28. Fossen, T.I. *Handbook of Marine Craft Hydrodynamics and Motion Control*; John Wiley & Sons: Hoboken, NJ, USA, 2011.
29. Carrica, P.M.; Wilson, R.V.; Noack, R.W.; Stern, F. Ship motions using single-phase level set with dynamic overset grids. *Comput. Fluids* **2007**, *36*, 1415–1433. [\[CrossRef\]](#)
30. Yasukawa, H.; Yoshimura, Y. Introduction of MMG standard method for ship maneuvering predictions. *J. Mar. Sci. Technol.* **2015**, *20*, 37–52. [\[CrossRef\]](#)
31. Abkowitz, M.A. *Measurement of Hydrodynamic Characteristics from Ship Maneuvering Trials by System Identification*; Society of Naval Architects and Marine Engineers: Jersey City, NJ, USA, 1980.

32. Park, J.; Rhee, S.H.; Yoon, H.K.; Lee, S.; Seo, J. Effects of a propulsor on the maneuverability of an autonomous underwater vehicle in vertical planar motion mechanism tests. *Appl. Ocean Res.* **2020**, *103*, 102340. [[CrossRef](#)]
33. Okuda, R.; Yasukawa, H.; Matsuda, A. Validation of maneuvering simulations for a KCS at different forward speeds using the 4-DOF MMG method. *Ocean Eng.* **2023**, *284*, 115174. [[CrossRef](#)]
34. Kim, D.-H.; Seo, J.; Kim, M.; Ha, J.; Park, G.; Rhee, S.H. Off-axial force and moment modeling of a marine propeller in oblique inflow by URANSE simulation. *Ocean Eng.* **2025**, *327*, 120993. [[CrossRef](#)]

Disclaimer/Publisher's Note: The statements, opinions and data contained in all publications are solely those of the individual author(s) and contributor(s) and not of MDPI and/or the editor(s). MDPI and/or the editor(s) disclaim responsibility for any injury to people or property resulting from any ideas, methods, instructions or products referred to in the content.